Neuron

Article

# Brain microvasculature has a common topology with local differences in geometry that match metabolic load

## Graphical Abstract

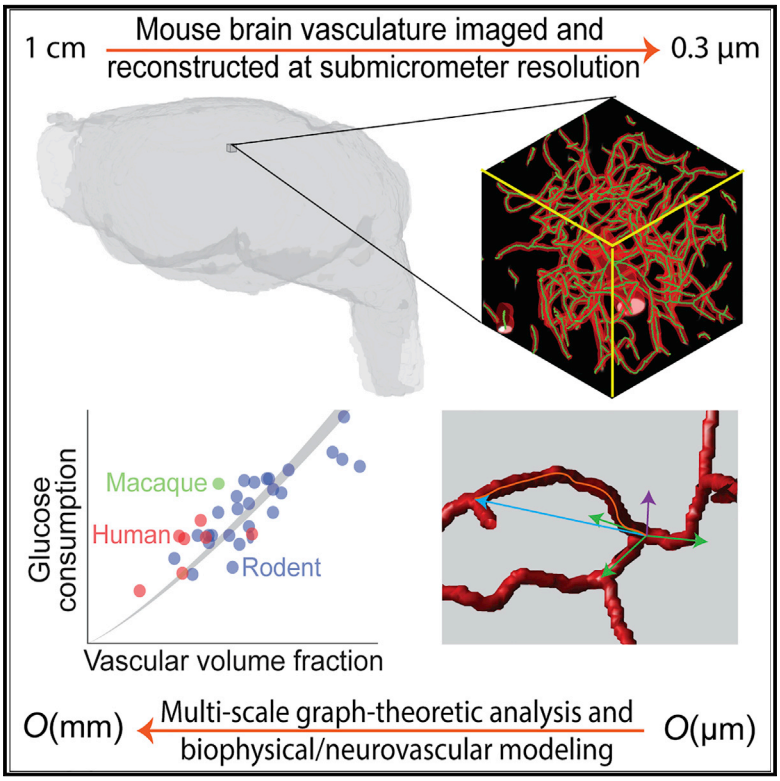


## Authors

Xiang Ji, Tiago Ferreira, Beth Friedman, ..., Erhan Bas, Jayaram Chandrashekar, David Kleinfeld

## Correspondence

dk@physics.ucsd.edu

## In brief

Ji et al. constructed the whole mouse brain microvascular connectome. Their analysis reveals a common network topology that leads to shared robustness against vessel rarefaction and stalled RBCs, while a heterogeneous network geometry matches the rate of regional resting metabolism to maintain a common maximum oxygen tension throughout the brain.

## Highlights

- Whole mouse brain microvascular connectome at sub-micrometer resolution
- Common network topology leads to a shared structural robustness against damage
- Regional network geometry linked to metabolism via diffusive transport of oxygen
- Large fraction of brain microvasculature is significantly anisotropic

Ji et al., 2021, Neuron *109*, 1–20
April 7, 2021 
https://doi.org/10.1016/j.neuron.2021.02.006

CellPress

Neuron

CellPress

Article

# Brain microvasculature has a common topology with local differences in geometry that match metabolic load

Xiang Ji,[1] Tiago Ferreira,[2] Beth Friedman,[3] Rui Liu,[1] Hannah Liechty,[1] Erhan Bas,[2,5] Jayaram Chandrashekar,[2] and David Kleinfeld[1,4,6,*]

[1]Department of Physics, University of California, San Diego, La Jolla, CA 92093, USA
[2]Howard Hughes Medical Institute, Janelia Research Campus, Ashburn, VA 20147, USA
[3]Department of Computer Science and Engineering, University of California, San Diego, La Jolla, CA 92093, USA
[4]Section of Neurobiology, University of California, San Diego, La Jolla, CA 92093, USA
[5]Present address: Amazon Web Services, Seattle, WA 98101, USA
[6]Lead contact
*Correspondence: dk@physics.ucsd.edu
https://doi.org/10.1016/j.neuron.2021.02.006

## SUMMARY

The microvasculature underlies the supply networks that support neuronal activity within heterogeneous brain regions. What are common versus heterogeneous aspects of the connectivity, density, and orientation of capillary networks? To address this, we imaged, reconstructed, and analyzed the microvasculature connectome in whole adult mice brains with sub-micrometer resolution. Graph analysis revealed common network topology across the brain that leads to a shared structural robustness against the rarefaction of vessels. Geometrical analysis, based on anatomically accurate reconstructions, uncovered a scaling law that links length density, i.e., the length of vessel per volume, with tissue-to-vessel distances. We then derive a formula that connects regional differences in metabolism to differences in length density and, further, predicts a common value of maximum tissue oxygen tension across the brain. Last, the orientation of capillaries is weakly anisotropic with the exception of a few strongly anisotropic regions; this variation can impact the interpretation of fMRI data.

## INTRODUCTION

Neuronal computations in the brain require a large and relatively continuous source of energy (Dienel, 2019). Glucose, oxygen, and other substrates and signaling molecules are transported by an extensive system of blood vessels that course throughout the brain (Mchedlishvili, 1986; Shih et al., 2015). The flow of blood is modulated by a multiplicity of neuronal and vascular mechanisms (Attwell et al., 2010; Iadecola, 2004; Kleinfeld et al., 2011), yet the modulation of flow is modest in the healthy brain. Flow increases by no more than a third of its baseline level upon sensory stimulation (Drew et al., 2010; Lee et al., 2001), albeit greater increases can occur during sleep (Bergel et al., 2018; Turner et al., 2020). The connection between vascular architecture and system-level brain energetics (Craigie, 1920), as well as the interpretation of fMRI (Di et al., 2013), is a long-standing question (Attwell and Laughlin, 2001). Here we focus on the reconstruction and analysis of microvascular networks, as these are the primary sites of exchange of energy substrates in the brain.

Past work provided complete reconstructions of vasculature with anatomically correct geometry for selected regions of human (Cassot et al., 2006), mouse (Blinder et al., 2013; Reichold et al., 2009), and marmoset (Guibert et al., 2012) neocortex. These data provided a means to estimate cortical blood flow (Blinder et al., 2013; Gould et al., 2017; Schmid et al., 2017) and ascertain the relation between vascular and neuronal density (Blinder et al., 2013; Guibert et al., 2012; Schmid et al., 2019; Tsai et al., 2009). More recent studies have completed brain-wide imaging of the vasculature (Kirst et al., 2020; Todorov et al., 2020; Xiong et al., 2017). These and some earlier studies (Boero et al., 1999; Craigie, 1920) have revealed variations in the density of vessels across different brain areas (Table 1) and have highlighted the effect of large-scale insults, such as stroke on vascular remodeling (Kirst et al., 2020). While highly informative, current reconstructions do not provide full connectivity among the vessels across brain region nor proper capillary radii; this precludes topological and geometrical analysis.

''Exact'' reconstruction of the vasculature is fraught with challenges. As a matter of sample preparation, all vessels must be fully labeled down to the finest capillaries. Morphological changes from fixation and embedding must be minimized and quantified. As a matter of microscopy, the entire brain needs to be imaged at sub-micrometer resolution for accurate assessment of capillary radii. In particular, estimates of flow dynamics require knowledge of capillary radii at the sub-micrometer scale in light of the steep dependence of flow resistance to vessel

**Table 1. Comparison with related works**

| | | This study | Kirst et al., 2020 | Todorov et al., 2020 | Xiong et al., 2017 | Wu et al., 2014 | Blinder et al., 2013 | Tsai et al., 2009 | Boero et al., 1999 | Craigie, 1920 |
|---|---|---|---|---|---|---|---|---|---|---|
| Data acquisition | Imaging | serial two-photon microscopy | lightsheet on hemisphere | lightsheet on whole brain | MOST | MOST | serial two-photon microscopy | serial two-photon microscopy | sections | sections |
| | Voxel size ($\mu m^3$) | 0.30 × 0.30 × 1.0 | 1.6 × 1.6 × 1.6 | 1.6 × 1.6 × 3.0 | 0.35 × 0.35 × 1.0 | 0.35 × 0.40 × 1.0 | 1.0 × 1.0 × 1.0 | 1.0 × 1.0 × 1.0 | – | – |
| | Labeling | lumen perfusion (FITC) | Acta 2, CD31, podocalyxin | Evans blue, wheat germ agglutinin | modified Nissl staining | modified Nissl staining | lumen perfusion (FITC) | lumen perfusion (FITC) | Nissl staining, silver emulsion | lumen perfusion (carmin gelatin) |
| | Clearing | index matching | iDISCO+ | 3DISCO | – | – | – | Triton X-100 plus sucrose | – | – |
| | Sample size | whole brain | hemisphere | whole brain | whole brain | whole brain | vibrissa cortex | vibrissa cortex | – | – |
| | *In vivo / in vitro* comparison | yes | – | – | – | yes | – | yes | – | – |
| Reconstruction | Segmentation resolution (μm) | 1.0 | 1.6 | 3.0 | 0.35 | 0.35 | 1.0 | 1.0 | – | – |
| | Radius estimation resolution (μm) | 0.25 | 1.6 | 3 | 0.35 | 0.35 | 1.0 | 1.0 | – | – |
| | Reconstruction scale | whole brain | hemisphere | whole brain | selected regions | selected regions | vibrissa cortex | vibrissa cortex | – | – |
| | Spatial graph representation | whole brain | hemisphere | – | – | – | vibrissa cortex | – | – | – |
| | Graph refinement | classifier based | end-point tracing | – | – | – | classifier based | – | – | – |
| Whole brain statistics | Number of nodes (N) | 4,132,583 | 3,200,000 | – | – | – | – | – | – | – |
| | Number of branches (B) | 6,320,303 | 4,400,000 | – | – | – | – | – | – | – |
| | Average (B/N) | 1.53 | 1.38 | – | – | – | – | – | – | – |
| | Number of branches in largest component | 6,238,701 | – | – | – | – | – | – | – | – |
| | Brain volume ($mm^3$) | 443 | 1,000 | 424 | – | 402 | – | – | – | – |
| | Total length per brain (m) | 384 | 288 | – | – | – | – | – | – | – |
| | Average length density ($m/mm^3$) | 0.867 | 0.288 | 0.546 | – | – | – | – | – | – |
| | Average vessel radius (μm) | 2.7 | 4 | 8 | – | – | – | – | – | – |

(*Continued on next page*)

**Table 1.** ***Continued***

| | | This study | | Kirst et al., 2020 | Todorov et al., 2020 | Xiong et al., 2017 | Wu et al., 2014 | Blinder et al., 2013 | Tsai et al., 2009 | Boero et al., 1999 | Craigie, 1920 |
|---|---|---|---|---|---|---|---|---|---|---|---|
| Regional vascular length density, $\rho_L$ m/mm$^3$) | | Vessel | Capillary | Vessel | Vessel | Capillary | Vessel | Vessel | Vessel | Capillary | Vessel |
| | Somatosensory cortex | 1.01 ± 0.02 | 0.98 ± 0.02 | 0.41 | 0.91 ± 0.09 | – | – | – | – | 1.07 | – |
| | Vibrissa cortex | 1.00 ± 0.03 | 0.97 ± 0.03 | 0.42 | 0.63 ± 0.09 | 0.98 | 0.88 | – | 0.88 ± 0.17 | – | – |
| | Auditory cortex | 0.95 ± 0.01 | 0.92 ± 0.01 | 0.33 | 0.77 ± 0.14 | – | – | – | – | 0.86 | – |
| | Motor cortex | 0.93 ± 0.03 | 0.91 ± 0.03 | 0.37 | 0.74 ± 0.12 | – | – | – | – | 0.87 | – |
| | Visual cortex | 0.85 ± 0.02 | 0.82 ± 0.02 | 0.33 | 0.73 ± 0.11 | – | – | – | – | 0.78 | – |
| | Hippocampus | 0.71 ± 0.03 | 0.68 ± 0.02 | 0.30 | – | 0.69 | – | – | – | – | – |
| | Ammon's horn | 0.68 ± 0.02 | 0.65 ± 0.02 | 0.32 | 0.49 ± 0.02 | – | – | – | – | – | – |
| | CA1 | 0.66 ± 0.03 | 0.63 ± 0.02 | 0.33 ± 0.01 | – | – | – | – | – | 0.58 | – |
| | CA3 | 0.71 ± 0.03 | 0.68 ± 0.03 | 0.33 ± 0.01 | – | – | – | – | – | 0.56 | – |
| | Caudoputamen | 0.85 ± 0.03 | 0.82 ± 0.03 | 0.41 ± 0.01 | 0.58 ± 0.06 | – | – | – | – | 0.49 ± 0.10 | – |
| | Thalamus | 1.04 ± 0.08 | 1.00 ± 0.08 | 0.49 | – | 0.95 | – | – | – | – | – |
| | Hypothalamus | 0.77 ± 0.03 | 0.74 ± 0.03 | 0.38 | 0.49 ± 0.14 | 0.66 | – | – | – | – | – |
| | Brainstem | 0.97 ± 0.04 | 0.93 ± 0.04 | 0.46 | 0.47 ± 0.05 | – | – | – | – | – | – |
| | Midbrain | 0.97 ± 0.06 | 0.93 ± 0.05 | 0.43 | 0.60 ± 0.04 | – | – | – | – | – | – |
| | Inferior colliculus | 1.46 ± 0.04 | 1.41 ± 0.04 | 0.71 ± 0.01 | 0.81 ± 0.08 | – | – | – | – | – | – |
| | Superior colliculus | 0.97 ± 0.06 | 0.92 ± 0.06 | 0.42 | – | 0.88 | – | – | – | 0.54 | – |
| | Pons | 0.97 ± 0.04 | 0.93 ± 0.03 | 0.54 | 0.31 ± 0.06 | – | – | – | – | – | – |
| | Medulla | 1.03 ± 0.02 | 0.98 ± 0.02 | 0.48 | 0.36 ± 0.09 | – | – | – | – | – | – |
| | Medial vestibular nucleus | 1.48 ± 0.08 | 1.41 ± 0.07 | 0.77 ± 0.02 | – | – | – | – | – | – | 1.36 ± 0.04 |
| | Dorsal cochlear nucleus | 1.46 ± 0.08 | 1.39 ± 0.07 | 0.68 ± 0.03 | – | – | – | – | – | – | 1.47 ± 0.04 |
| | Superior olive | 1.42 ± 0.04 | 1.37 ± 0.04 | 0.76 | – | – | – | – | – | – | 1.12 ± 0.04 |
| | Lateral vestibular nucleus | 1.02 ± 0.19 | 0.98 ± 0.19 | 0.58 ± 0.02 | – | – | – | – | – | – | 0.93 ± 0.03 |
| | Cerebellum | 1.10 ± 0.05 | 1.06 ± 0.04 | 0.63 | 0.47 ± 0.05 | – | – | – | – | 1.20 | 1.11 |
| | Dentate nucleus | 1.49 ± 0.12 | 1.45 ± 0.11 | 0.78 ± 0.08 | – | – | – | – | – | – | 1.27 ± 0.03 |

For Kirst et al. (2020): (1) brain volume = (3.2 × 10$^6$ nodes per hemisphere × 2) ÷ (average node density 6,400 / mm$^3$) = 1,000 mm$^3$; (2) total vessel length per brain = (144 ± 2) m per hemisphere × 2 = (288 ± 4) m; (3) average length density = 288 m ÷ 1,000 mm$^3$ = 0.288 m/mm$^3$; (4) average vessel radius is estimated from their Figures 4G, S3H, and S6C; (5) regional vessel length densities are from their Figure 4B or by averaging over the included subregions. For Todorov et al. (2020): (1) average vessel radius is estimated from their Figure 5C; (2) regional length densities were computed from supplemental data for C57BL/6 mice. For Xiong et al. (2017): regional length densities are estimated from their Figure 9E. For Boero et al. (1999) and Craigie (1920): estimated regional length densities are averages of the included subregions. Error bars represent standard error.

Please cite this article in press as: Ji et al., Brain microvasculature has a common topology with local differences in geometry that match metabolic load, Neuron (2021), https://doi.org/10.1016/j.neuron.2021.02.006



radius (Secomb et al., 1998). With regard to analysis, the topological and geometrical properties of the whole-brain vascular network remain to be quantified. An unresolved challenge posed by past observations (Borowsky and Collins, 1989; Weber et al., 2008) is to delineate how transport depends on the length of blood vessel per volume in different brain regions. Determination of vessel length densities will therefore enable determination of scaling laws to relate substrate transport to vascular geometry.

Here we ask which aspects of whole brain capillary organization are either identical or distinct in different brain regions. (1) Is the topology of the network, such as how vessels meet and interconnect, the same across different brain regions? If so, does this imply an invariant percolation threshold, i.e., a fraction of vessels that can be lost before the network fractures into disconnected regions (Hudetz, 1993)? The answer bears on potential debilitating effects from cortical capillaries with stalled blood flow, which is enhanced in Alzheimer's disease brains (Cruz Hernández et al., 2019). (2) How does vascular length density of capillaries vary across brain regions? In particular, is there a simple relation between length density and the distance between locations in the parenchyma and the nearest vessel? (3) Further, do region specific variations in vascular length density relate to published differences in regional glucose utilization (Hawkins et al., 1985)? (4) Are there regional variations in the preferred orientation of capillaries across brain regions (Buxton et al., 2014; Gagnon et al., 2015; Weber et al., 2008)?

## RESULTS

Complete filling of the vasculature is a balance between sufficient pressure to fill all vessels but not rupture vessels. We used a variant of a past technique (Tsai et al., 2009) to fill vessels with gelatin and fluorescein-conjugated bovine serum albumin and then cross-link these constituents to lumen proteins (STAR methods). As a control, we compared the same volume of labeled vessels in cortex after perfusion in the living animal (Figure S1). We found seven partially unfilled short segments among 2,835 vessel segments in 15 volumes across 3 animals; i.e., 0.998 of all microvessels had no discernable gap and the 0.002 of vessels had a gap of less than 10 $\mu m$.

Entire brains (three mice) were then extracted (Figure 1A), post-fixed, index matched, and imaged at 0.3 × 0.3 × 1 $\mu m^3$ voxel resolution (Economo et al., 2016). We roughly estimated the coordinates for the centerlines of small vessels and the lumen of larger vessels as a means to stitch all of the image stacks by a non-rigid transformation (Figure 1B). This led to a composite image of the entire brain at 0.25 × 0.25 × 1.0 $\mu m^3$ voxel size with optical distortion and local tissue deformation largely eliminated (Figure 1C). The composite image is downsampled to 1 $\mu m$ isotropic voxel resolution and divided into cubes that are 240 $\mu m$ on edge, denoted 240-cubes, with a 208 $\mu m$ pitch in Cartesian coordinates (Figure 1D). Each brain is covered by about 50,000 of the 240-cubes.

### Extracting an annotated graph that preserves physical dimensions

See STAR methods and the MATLAB implementation in Methods S1 for details of all numerical procedures.

### Segmentation

The first step is to label each voxel in the imaging data as a potential vessel or as void. We remove shot-noise with a median filter, then perform two complementary computations on each 240-cube and take the intersection of the outputs. One computation is to apply a matched filter for rods (Tsai et al., 2009) followed by a Frangi vesselness filter (Frangi et al., 1998) to select for voxels that are likely part of vessels. The second computation is to threshold the values in each 240-cube with respect to a level that selects for voxels with a relatively high intensity. We then take the overlap of the two computations. Last, we agglomerate neighboring pixels with a high signal-to-noise ratios and discard small clusters of voxels. The result is a refined classification of voxels as either potential vessels or void.

### Skeletonization and graph construction

An initial estimate of the centerline of the vessels was computed by a topology-preserving thinning algorithm (Lee and Kashyap, 1994). The centerlines were found for clusters of nominally 5 × 5 × 5 of the 240-cubes with a pitch of 3 of the 240-cubes and were refined by local operations. Each of the voxels in the centerline was compared against that of neighboring voxels. The centerline was shifted to the neighbor if the neighbor had higher intensity and the shift preserved the topology of the network (blue green voxels, Figure 1E). Each voxel on a centerline was then classified as either an isolated voxel, an endpoint voxel with one neighbor, a link voxel that connects two neighbors, or a node voxel with three or more neighbors among their $3^3$–1 possible neighbors. Finally, the associated radius was assigned as the distance from the voxel to the nearest boundary between vessel and void. This forms a primitive vascular graph.

### Graph refinement

We trained random forest classifiers to perform whole-brain automatic graph refinement. This involved removal of isolated voxels, short segments with one or two endpoint voxels (Figure 1F), and false positive connections (Figure 1G). It further involved the addition of segments of voxels to bridge free-ended segments and form a contiguous centerline (Kaufhold et al., 2012; Figures 1H and 1I). The classifiers achieved more than 0.95 fractional accuracy with respect to manual annotation (Table S1). As a measure of the improved structural accuracy, a fraction 0.49 of the 240-cubes that did not include an outer brain surface also did not contain any vessel segments with an endpoint (Figure 1J). Last, we inspected the reconstructed microvascular network in six, randomly selected 240-cubes from different brain regions and found three connectivity errors out of 2,133 vessel segments; i.e., 0.999 of the vessels are free of errors in connectivity (Figure S1).

### Super-resolution vessel radius estimation

A nested, iterative procedure was developed to improve the estimate of the radius of each vessel by processing the 0.25 μm lateral resolution images (Figure 2A). We first formed a look-up table of the expected intensity profile, denoted $I = I(x, y, z; r, \theta, \omega_{xy}, \omega_z)$, for a vessel in terms of four parameters: the vessel radius, denoted $r$, the elevation angle with respect to the focal plane, denoted $\theta$, and three-dimensional Gaussian point spread

Please cite this article in press as: Ji et al., Brain microvasculature has a common topology with local differences in geometry that match metabolic load, Neuron (2021), https://doi.org/10.1016/j.neuron.2021.02.006





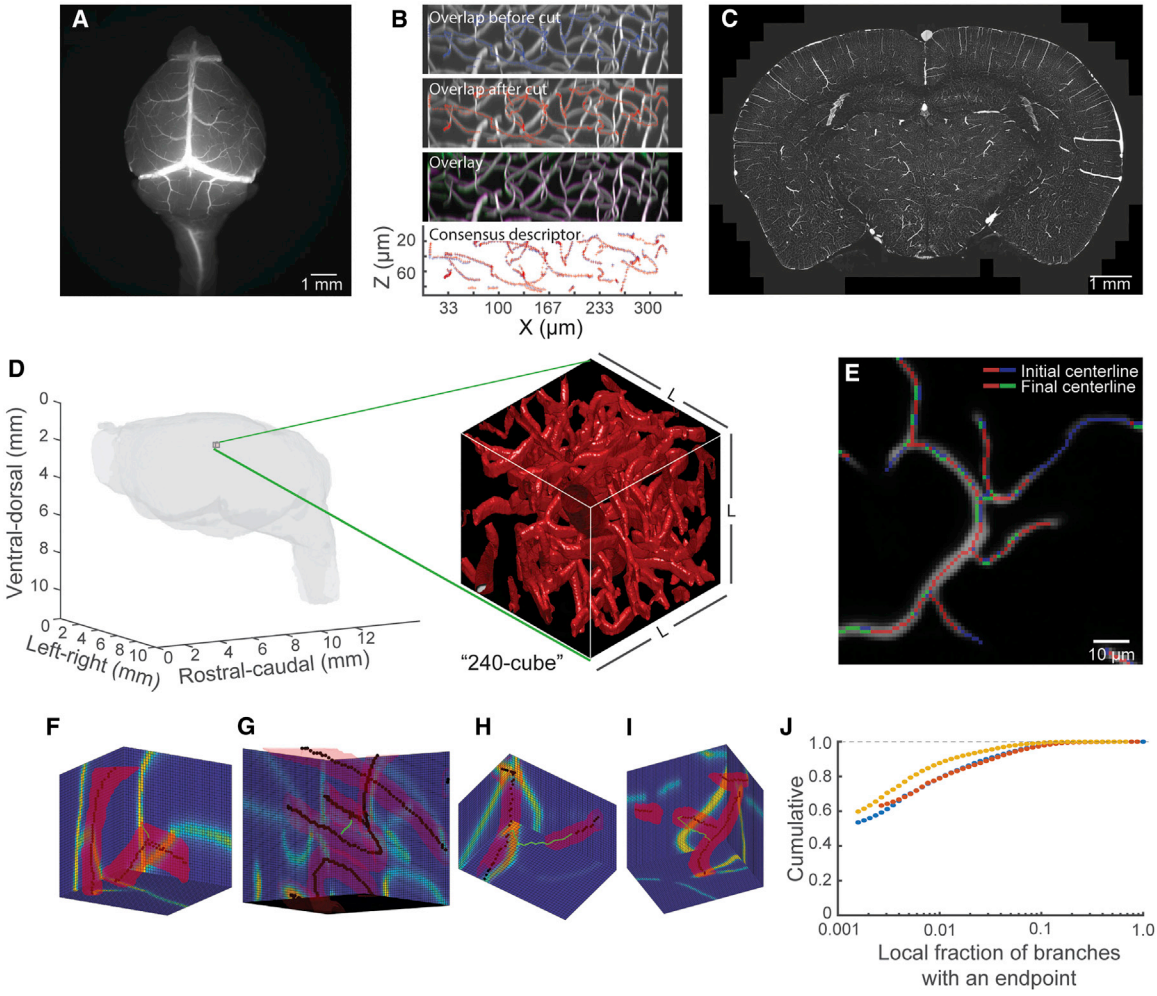


**Figure 1. Sample preparation, imaging, image processing, and vascular graph reconstruction**

(A) Photomicrograph of a whole mouse brain with vessel lumen filled with fluorescent gel.

(B) Vessel skeleton voxels in the overlapping volume of adjacent image tiles in z-direction were matched to compute the nonrigid transformation for image stitching. The entire brain consists of about 20,000 partially overlapping images stacks.

(C) Maximum intensity projection image of a 100-μm-thick slab of brain after stitching.

(D) Mask of the whole mouse brain with vessel segmentation in one of the $L^3 = (240\ \mu m)^3$ image volumes; these are denoted as "240-cube."

(E) Illustration of vessel centerline adjustment. Centerline voxels were moved to a neighboring position with higher intensity if the adjustment preserved the topology. Unmoved voxel: red. Moved voxel before adjustment: blue. Moved voxel after adjustment: green.

(F–I) Illustration of candidate vessel segments for the graph refinement procedure. The reconstructed vessels are in red, the neighboring centerlines are in black, and the segments to be classified are in green. Note the presence of the maximum projections along the surfaces of the cube. (F) A vessel segment with one free endpoint that needs to be removed. (G) A false positive connection that results from relatively low axial imaging resolution and proximity of vessels. (H) A correctly proposed linker that needs to be added to the centerline. (I) An incorrectly proposed linker that should not be added.

(J) Cumulative distribution function of the fraction of vessel segments in 240-cubes that have at least one endpoint voxel. On average, 0.485 of the 240-cubes that are completely inside the brain do not have any open-ended vessel segment.

function (PSF). The elevation angle of the vessel is readily determined from the skeletonization procedure and used without further modification. The PSF is characterized by lateral and axial half-widths-at-half-maximum intensity, denoted $\omega_{xy}$ and $\omega_z$, respectively (insert, Figure 2B). For each brain, we estimated the PSF near tens of thousands of voxels along the centerline and found relatively consistent values of the widths across different brain regions (Table S2; Figure S2). The different profiles $I$ were computed as the convolution between a vessel lumen with uniform fluorescence intensity and a three-dimensional Gaussian PSF (Figure 2B). The intensity at the edge of a vessel, denoted $I_r$ at point $(x,y,z) = (0,r,0)$ in the insert of Figure 2B, changes as both lateral and axial resolution decrease and depends nonlinearly on vessel radius and elevation angle (Figures 2B and 2C). The intensity at an edge is least sensitive to changes in radius when the vessel lies in the axial direction and is highly sensitive to changes for vessels that lie in the focal plane.

Please cite this article in press as: Ji et al., Brain microvasculature has a common topology with local differences in geometry that match metabolic load, Neuron (2021), https://doi.org/10.1016/j.neuron.2021.02.006



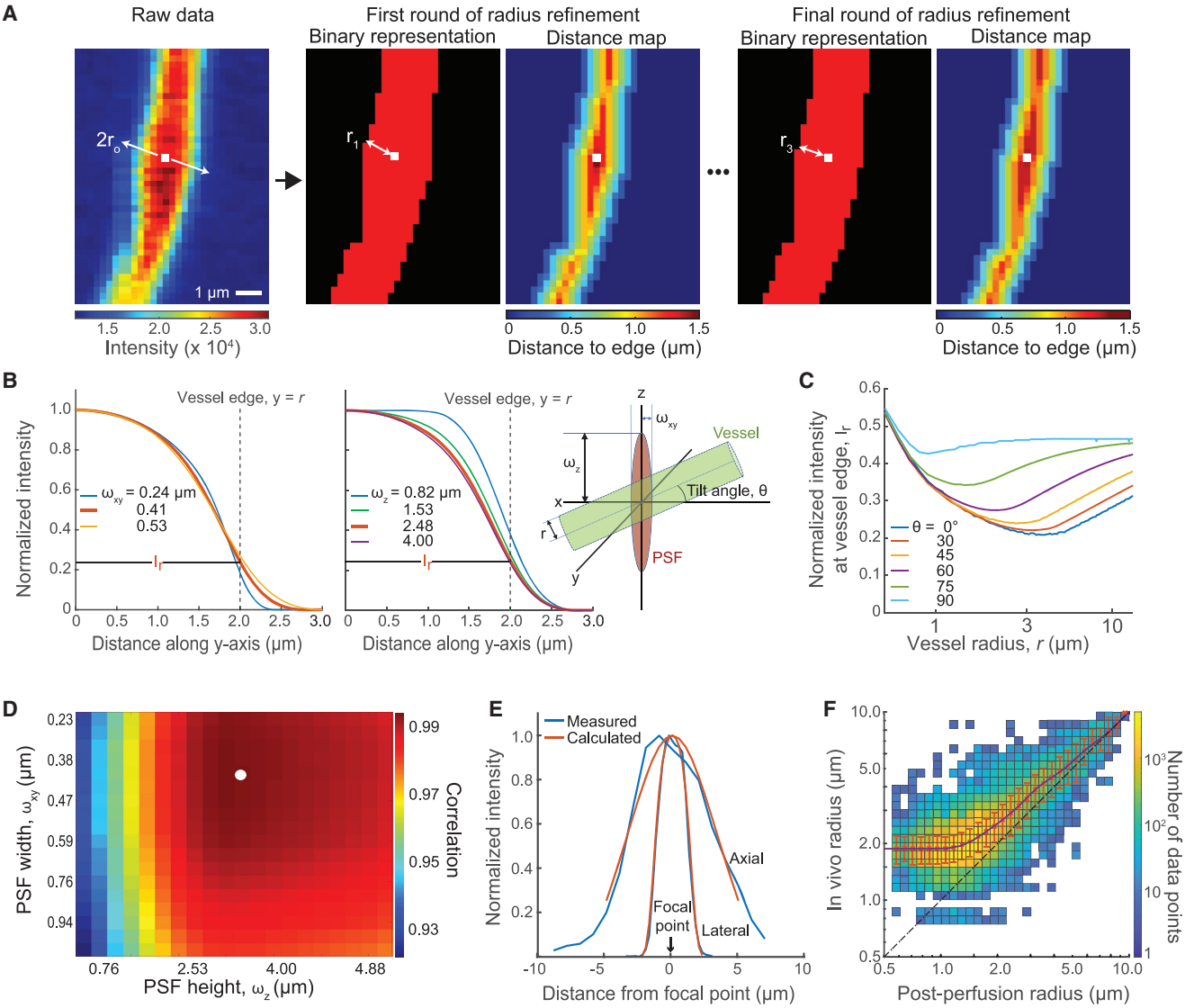


**Figure 2. Super-resolution estimation and calibration of vessel radius**

(A) Determination of the radius associated with a voxel that lies at the centerline (white square) of the vessel. Iterative progression from raw data to final super-resolution estimate of the radius. The raw data have the centerline tilted at $\theta = 6°$ and an initial estimate $r_0 = 2$ μm. Then, the initial super-resolution estimate of $r_1$ is determined by thresholding the intensity profile of the raw data at the value of $I_{r_0}$ **(C)**, which leads to the new estimate, read from the distance map, of $r_1 = 1.46$ μm. This process is repeated until the radius converges to a final value of 1.35 μm.

(B) Calculated normalized horizontal radial light intensity profile of a vessel. The profile is along the y axis of the vessel in the insert, with $\theta = 0°$ and $r = 2.0$ μm, for a PSF of the beam with different $\omega_{xy}$ ($\omega_z = 3.4$ μm; left) and different $\omega_z$ ($\omega_{xy}$0.41 μm; right), respectively

(C) Normalized horizontal vessel edge intensity for vessels of different radius and orientation ($\omega_{xy} = 0.44$ μm and $\omega_z = 3.4$ μm).

(D) Estimation of the PSF. We numerically searched for parameters that maximized the weighted-average normalized correlation between the simulated intensity profiles and the actual profile. The white dot shows the optimal PSF parameters at one centerline voxel ($\omega_{xy} = 0.41$ μm, $\omega_z = 3.4$ μm).

(E) Measured (blue) and simulated (red) lateral and axial intensity for the optimum PSF parameter found in (D); vessel fitted radius is $r = 1.6$ μm. The weighted-average normalized correlation is 0.995.

(F) Joint distribution of *in vivo* vessel radius versus post-perfusion vessel radius of matched vessel centerline voxels from 6 mice. The solid curve is the median of *in vivo* radius binned according to post-perfusion radius. The error bar shows middle quartiles.

The skeletonization procedure estimated the radius of a vessel with a resolution of 1 μm (Figure 2A). This radius, denoted $r_0$, was refined by thresholding the intensity profile of the raw data at the value of $I_{r_0}$, which leads to a new estimate of radius, denoted $r_1$. As a practical matter, the estimate of the radius is determined from a map of the shortest distance to the lumen wall from inside the vessel, the so-called "distance map." The radius is further refined by thresholding the intensity profile of the raw data at the value of $I_{r_1}$. This process is continued until the estimate of the radius converges, typically by three iterations ($r_3$ in Figure 2A).

Please cite this article in press as: Ji et al., Brain microvasculature has a common topology with local differences in geometry that match metabolic load, Neuron (2021), https://doi.org/10.1016/j.neuron.2021.02.006



CellPress

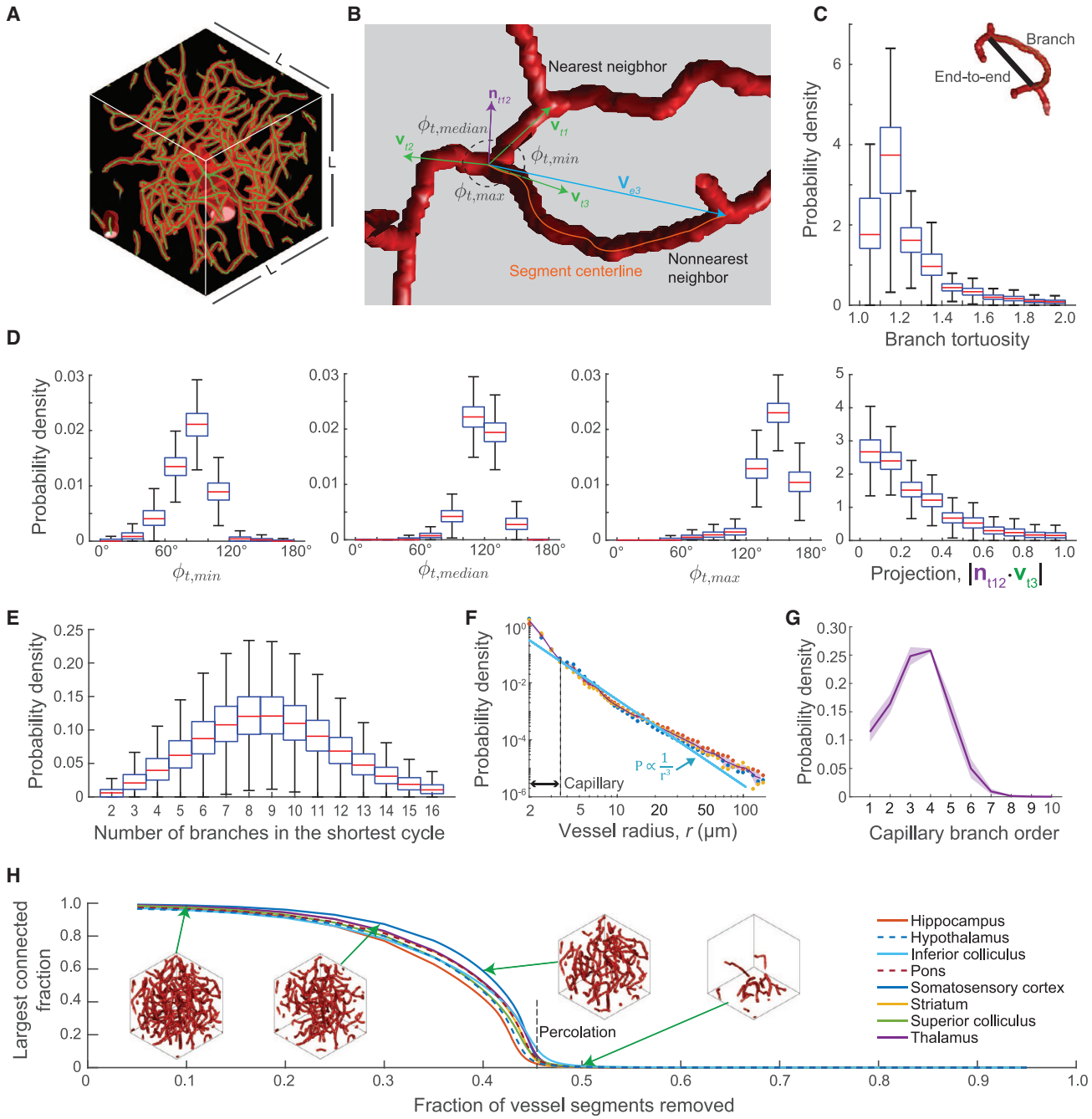


**Figure 3. Common network topology and branch and node geometry across all brains**

(A) Reconstructed vessel mask (red tubes) with centerlines (green curves) in one 240-cube.

(B) Reconstructed rendering of a small segment of the vascular network highlighting angles at a triadic node.

(C) The probability density function (PDF) of the vessel branch tortuosity. The insert shows a vessel segment of tortuosity 1.27, which is the ratio between the length of the branch (red) and the end-to-end distance (black). Each whisker shows the distribution of the probability density in the bin for all the 240-cubes within the brains, outliers not shown, same as (D) and (E).

(D) The PDFs for the smallest, median, and largest branch tangent angle of vessels joined at a node, along with the cosine of the elevation angle between the third tangent vector and the plane spanned by the first two tangent vectors. The average value of $\phi_{t,min}$, $\phi_{t,median}$, and $\phi_{t,max}$ are 84 ± 4°, 118 ± 2°, and 145 ± 3° (mean ± SE), respectively.

(E) The PDF of the number of branches in the shortest cycle of vessels.

(F) The PDF of the radius distribution for all vessels for all three brains (red, yellow, and blue dots); the mean (solid) and standard deviation (shadow) are in purple. The mean value of the radius is 2.74 ± 0.09 μm (mean ± SD), and the median is 2.14 ± 0.04 μm. The power law (blue line) has a slope of −3.

*(legend continued on next page)*

Please cite this article in press as: Ji et al., Brain microvasculature has a common topology with local differences in geometry that match metabolic load, Neuron (2021), https://doi.org/10.1016/j.neuron.2021.02.006



We next refined our estimate of the PSF using the refined radii associated with the centerline points. For each centerline voxel, the new estimation of PSF parameters was determined by maximizing the correlation between the measured and calculated radial intensity profile along horizontal and axial directions, weighted by orientation (Figures 2D and 2E). The newly refined PSF was then used to re-calculate the look-up table for the $I(x, y; r, \theta, \omega_{xy}, \omega_z)$ (Figure 2C), and the radius of the vessel centerline was recalculated (Figure 2A). This process of nested iteration converged in two to three cycles and yielded a final estimate of the radius associated with each voxel on the centerline.

### *In vivo* radius calibration

We now turn to systematic errors in the estimation of the vessel radii in the living versus gel-perfused brain. We collected data from volumes of microvessels in parietal cortex using adaptive optics two-photon microscopy to image vessels in living animals with the blood plasma filled with fluorescein-dextran and, in the same animal, after perfusion with a fluorescein-gel. The PSF has 0.2 μm lateral resolution (Liu et al., 2019). We iteratively estimated the *in vivo* vessel radius using the same algorithm as for the gel-perfused brains. By registering the post-perfusion vessel skeleton voxels to the *in vivo* skeleton, we measured the change in radius at 102,284 positions (6 mice) to compute the radius calibration curve (Figure 2F). Vessels with radii less than ~ 5 μm shrunk after perfusion. We computed a calibration curve and applied it to convert the post-perfusion vessel radii to their inferred *in vivo* values. Of interest, the minimum *in vivo* vessel radius is 1.9 ± 0.3 μm (mean ± SD).

### Basic topology and geometry

The output of our pipeline is an annotated graph with branchpoints positioned at 1 μm resolution and the radii of vessels estimated at 0.25 μm resolution (Figure 3A). A derived graph of branches and nodes, with the branches labeled by the length of the centerline and the radius found as the median of the radii for all centerline voxels (Figure 3B), is formed from the annotated graph (Table 1; Table S2). On average, $(278 \pm 12)\times10^6$ (mean ± SD) centerline voxels form an undirected graph with $(6.32 \pm 0.27)\times10^6$ branches ($B$) and $(4.13 \pm 0.17)\times10^6$ nodes ($N$). We obtained 384 ± 16 m of vessel segments filling 443 ± 9 $mm^3$ of brain tissue after correcting for tissue shrinkage during the sample preparation (Figure S3). The largest graph connected component contains 0.987 ± 0.012 of the branches. Thus, virtually all of the reconstructed vessel segments form an interconnected network.

#### *Coordination*

The primary topological feature is the number of branches that join at each node, defined as the degree of the node. Across all 240-cubes, we found that branches dominantly jointed as triads, with 0.968–0.987 (middle quartiles) of the nodes being of degree 3 and an average degree 3.02 ± 0.02 across all brains. As a result, the branch-to-node ratio of 1.529 ± 0.004 (mean ± SD) is very close to the theoretical value of 3/2 for a mesh graph of degree 3. Virtually all branches are in a single connected component and virtually all branches connect exclusively as triads. Thus, the vessels form a highly redundant network with roughly $N/2$ independent loops, where the number of independent loops is the maximum number of branches that can be deleted before the network breaks into two connected components (Newman, 2010).

What is the geometry of the triads? If we join three randomly oriented straight lines in three dimensions, the distribution of angles between lines would fall into a unit sphere. To determine whether this holds for the angular distribution of the vasculature, we computed the end-to-end vector $\mathbf{v}_e$, endpoint tangent vectors $\mathbf{v}_t$, and the length $l$ of each vessel segment (Figure 3B). First, the ratio between the vessel length and the end-to-end distance $l_e = |\mathbf{v}_e|$, i.e., the tortuosity of the branch, is 1.27 ± 0.05 (mean ± SE) as an average over all 240-cubes (Figure 3C). Thus, vessels in the brain are fairly straight. Using the branch tangent vectors near the node, the average minimum, median, and maximum angle between branches, denoted as $\theta_{t,min}$, $\theta_{t,median}$, and $\theta_{t,max}$, were found to be 84° ± 4°, 118° ± 2°, and 145° ± 3°, respectively (Figure 3D). As two linearly independent vectors defined a plane with the normal vector $\mathbf{n}_{12}$ (Figure 3B), we also computed the absolute value of its projection onto the third vector. The average projection was 0.255 ± 0.037 and corresponds to a small average elevation angle of 14.8°. This implies that branches tend to stay in a plane near the branch point (Figure 3B).

#### *Loops*

Network topology can be further quantified by the number of branches in the shortest path that one needs to traverse to return to the same node. Relatively consistent distributions were found across the whole brain, with 8.97 ± 0.53 (mean ± SE) branches in the shortest loop (Figure 3E). Only about 0.011 (median) of the loops consist of only two branches, i.e., branches in parallel, which suggests the low frequency of matured brain vessels originate directly from intussusceptive angiogenesis.

#### *Compactness*

The interplay between Euclidean and geodesic distance, i.e., the minimum number of branches, between nodes indicates the compactness of the connectivity. We computed the pairwise Euclidean distance between pairs of nodes and counted the number of branches between the pairs. We find that 0.85–0.91 of the nodes were directly connected to its nearest node, while the other branches form non-nearest neighbor connections.

#### *Definition of capillaries*

Microvessels dominated the probability density function (PDF) of branch radius (Figure 3F), as anticipated. The PDF follows a power law decrement for radii larger than 3.5 μm (Figure 3F). We

(G) The PDF of the capillary branch order from the nearest penetrating vessels as an average over three brains.
(H) Catastrophic disassemble of regional vascular network after 0.44 of the vessel segments were randomly removed. Inserts were examples of the largest graph connected component visualized in a 240-cube. The standard deviation of the largest connected fraction is less than 0.02 for cases with less than 0.4 or greater than 0.5 of the vessel segments removed. The standard deviation increases to 0.05 near the threshold for disassembling the network. Brain regions were assigned using the Common Coordinate Framework (Wang et al., 2020).

Please cite this article in press as: Ji et al., Brain microvasculature has a common topology with local differences in geometry that match metabolic load, Neuron (2021), https://doi.org/10.1016/j.neuron.2021.02.006





classified vessel segments as capillary versus non-capillary based on the threshold radius of 3.5 μm for deviation from a power law; this will be further justified by additional analysis. Under this definition, capillaries comprise 0.8 ± 0.2 (mean ± SD) of the vascular volume with each 240-cube (Figure S4) and account for the vast majority, i.e., 0.959 ± 0.008, of the total vascular length.

The asymptotic power law has a scaling exponent of −2.73 ± 0.03 with $R^2$ = 0.98 for radii larger than 3.5 μm (Figure 3F). This exponent is close to that of −3 given by Murray's Law to minimize the cost required to drive the flow of liquids through a network of tubes and concurrently maintain the transportation system (Murray, 1926).

Starting from the non-capillaries, i.e., penetrating arterioles or venules, we iteratively labeled branches according to the geodesic distance to the nearest non-capillary segment. The capillary branches that are directly connected to non-capillaries were labeled as order 1, the unlabeled branches that are directly connected to order 1 branches were labeled as order 2, and so forth. The average capillary branch order was 3.4 ± 0.2 (mean ± SD) (Figure 3G), which suggests that penetrating arterioles and venules are typically bridged by capillary networks that have seven branches as their shortest path. Conversely, few capillaries are more than seven branches from a penetrating vessel, as shown previously (Kirst et al., 2020).

### *Structural basis of network robustness*

Common network topology implies a similar bond percolation threshold (Vyssotsky et al., 1961) across different brain regions. To test this, we randomly removed different fractions of the vessel branches and computed the fraction of remaining nodes in the largest graph connected component. In all the brain regions, the largest component rapidly broke into small graphs when 0.433–0.447 of the branches were removed (Figure 3H). Therefore, the bond percolation threshold was about 0.56. This is very close to the known bond percolation thresholds of 0.542–0.556 for triadic lattices (Tran et al., 2013). Thus, as a result solely of topology, the loss or stall of less than half of all capillaries will lead to a catastrophic failure of the vascular system.

## Anisotropy of the brain capillary networks

A long-standing question is whether the capillaries have a net orientation, particularly in regions where neuronal processes tend to co-align, or whether the capillaries form an isotropic bundle on the scale of identified brain regions (Báez-Yánez et al., 2017). The latter assumption has been used to estimate vascular density (Borowsky and Collins, 1989; Weber et al., 2008) and blood flow in magnetic resonance imaging (Fisel et al., 1991; Ogawa et al., 1993). To answer this question, we systematically quantified brain vessel anisotropy. End-to-end vectors of vessel branches, weighted by the volume of the vessel, were used to compute the correlation matrix of the relative orientations between all branches in each of the 240-cubes across all brains (Figures 4A and 4B; Video S1). The anisotropy was computed from the eigenvalues of the correlation matrix; a value of zero means that orientation is isotropic, while a value of one means that all capillaries are co-aligned. Statistical significance was estimated from Monte Carlo sampling (Figure 4C). As an average across all of the 240-cubes, the anisotropy was lowest, yet statistically significant and relatively constant at ~ 0.4 when vessels with radius at or below 3.5 μm were considered (Figure 4D); this corresponds to our cutoff for capillaries (Figure 3F).

The regional capillary anisotropy was visualized as an overlay in horizontal and sagittal projections, color-coded with the p value to indicate statistical significance (Figure 4E). The boundaries of brain regions were determined by registering brains to the Common Coordinate Atlas (Wang et al., 2020). Particularly striking anisotropy was observed within the superior colliculus along the dorsal—ventral axis, and within the pons along the caudal—rostral axis (Figure 4F). The corpus callosum also had high anisotropy, albeit with low statistical significance as a result of its relatively low density of vessels. Contrariwise, the inferior colliculus had low yet significant anisotropy. The anisotropy with neocortex varied with depth. Capillaries were found to preferentially lie normal to the pial surface within the superficial layers yet were only weakly oriented within the deep layers of cortex (Figure 4G).

## Descriptive statistics of regional capillary lengths

Different brain regions have different susceptibility to microstrokes and varying energetic loads. As the first step to elucidate the role of potential vascular geometry in explaining these differences, we examine the length density, denoted $\rho_L$, of capillaries. Qualitatively, selected brain slices indicate strong regional differences with a relatively high length density in neocortex, thalamus, and cerebellum (Figure 5A; Video S2). We next compute the PDF of $\rho_L$ in each major brain region as an average across hemispheres (3 mice) (Figure 5B; Table 1; Table S3). Three-fold differences in length density are observed, from $\rho_L$ = 0.49 ± 0.12 m/mm$^3$ (mean ± SE) in corpus callosum, a region dominated by white matter, to 1.41 ± 0.05 m/mm$^3$ in inferior colliculus, an auditory nucleus known for high neuronal activity (Gross et al., 1987).

The variation in capillary length density across the cortical mantle is modest. Neocortical regions, like somatosensory cortex, had higher average density than paleocortex regions, like piriform cortex, i.e., $\rho_L$ = 0.98 ± 0.02 m/mm$^3$ (mean ± SE) versus 0.72 ± 0.01 m/mm$^3$, respectively (Table 1). Consistent with past work (Blinder et al., 2013; Kirst et al., 2020; Tsai et al., 2009; Wu et al., 2014), the density within a multitude of neocortical areas varied weakly as a function of depth (Figure 5C). There is a peak in $\rho_L$ at approximately 400 μm below the pia for auditory, somatosensory, and visual areas, albeit no discernable peak for anterior cingulate cortex. In contrast to neocortex, the density in piriform cortex was highest in the superficial layers and decreased to a minimum value at approximately 400 μm below the pia (Figure 5C).

The difference in length density across regions is related to the difference in the distribution of the length of different capillary branches. Regions with high values of $\rho_L$, such as inferior colliculus and somatosensory cortex, have relatively more short branches, with median lengths of 45 ± 1 μm (mean ± SE) and 46 ± 1 μm, respectively. The corpus callosum, with relatively low density (Figure 5B), has significantly longer median branch lengths, i.e., 67 ± 3 μm. Interestingly, branches shorter than 40 μm dominate across the brain, while branches that extend beyond 200 μm are rarely observed (Figures 5D and 5E). All

Please cite this article in press as: Ji et al., Brain microvasculature has a common topology with local differences in geometry that match metabolic load, Neuron (2021), https://doi.org/10.1016/j.neuron.2021.02.006



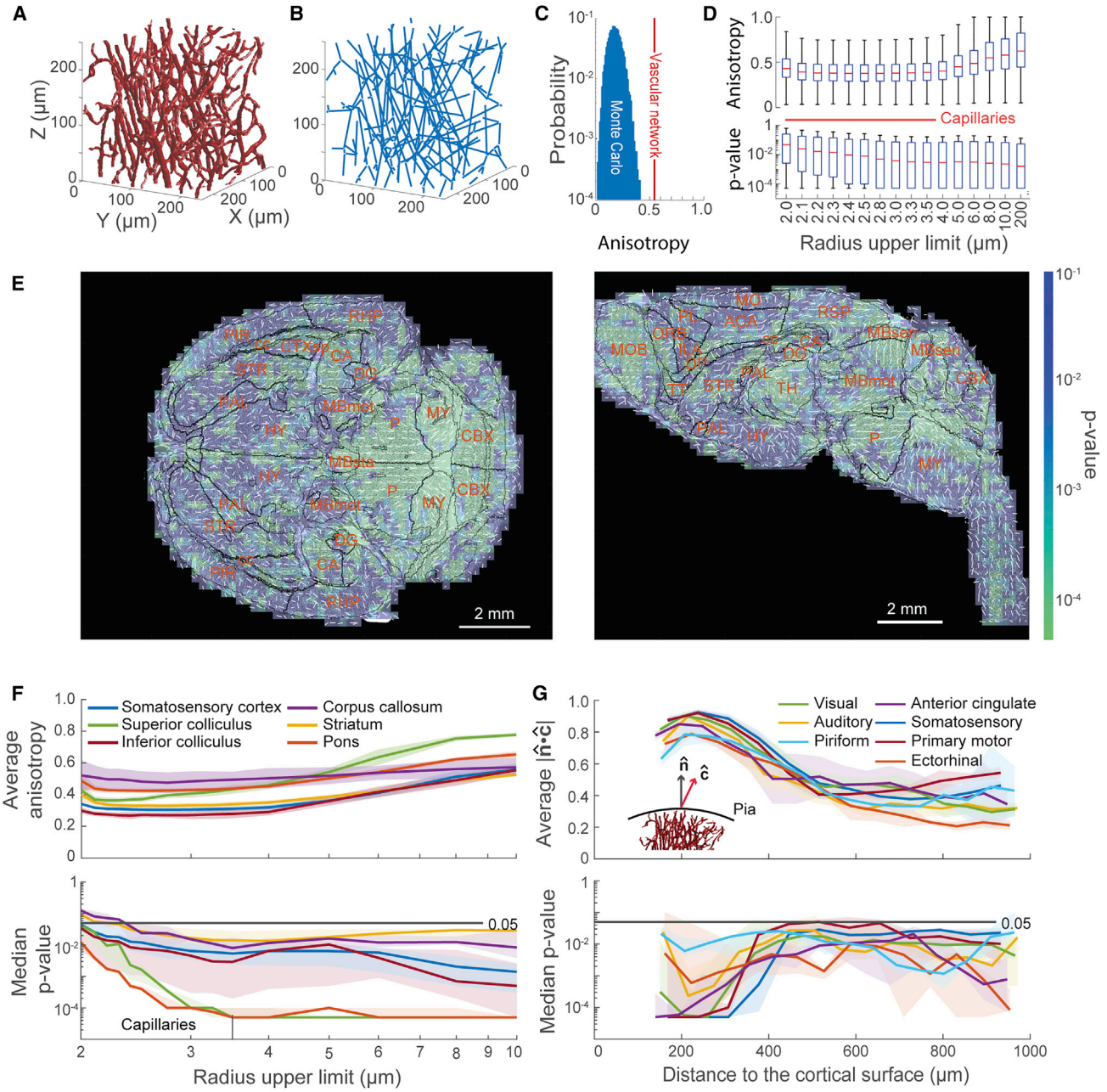


**Figure 4. Vascular network anisotropy**

(A) The reconstructed vascular network in a 240-cube.

(B) Abstracted vessel segments drawn as endpoint-to-endpoint straight lines.

(C) Volume-weighted local vascular network fractional anisotropy computed from the lines in (B) (red vertical line) and the distribution of anisotropy computed from the same number of randomly orientated vessels with the same volume weights (blue histogram; 10,000 trials).

(D) The anisotropy distribution across 240-cubes in two brains, along with statistically significant (p value), as a function of the maximum vessel radius included. Median p value is $p < 0.01$ down to radii of 2.4 μm. All p values smaller than $10^{-4}$ are set to $5\times10^{-5}$ for visualization purposes, same as (E)–(G).

(E) Local capillary (radius ≤3.5 μm) anisotropy statistical significance (p value) and preferred orientation (white lines) overlaid on a 240-μm-thick maximum projection of reconstructed vessels. Black curves and red labels indicate regional contours and name abbreviations according to Allen Atlas. Full names for the abbreviations are summarized in Table S4.

(F) The radius dependence of the average anisotropy, including standard error bands, and associated median p values, including 0.25–0.75 bounds over 4 hemispheres.

(G) Cortical depth dependence of the average orientation of capillaries, including standard error bands, and associated median p values within a region, including 0.25–0.75 bounds. The plotted data are the mean orientation ($\hat{\mathbf{c}}$) projected onto the normal to the cortical surface ($\hat{\mathbf{n}}$) as an average over 4 hemispheres.

Please cite this article in press as: Ji et al., Brain microvasculature has a common topology with local differences in geometry that match metabolic load, Neuron (2021), https://doi.org/10.1016/j.neuron.2021.02.006



CellPress

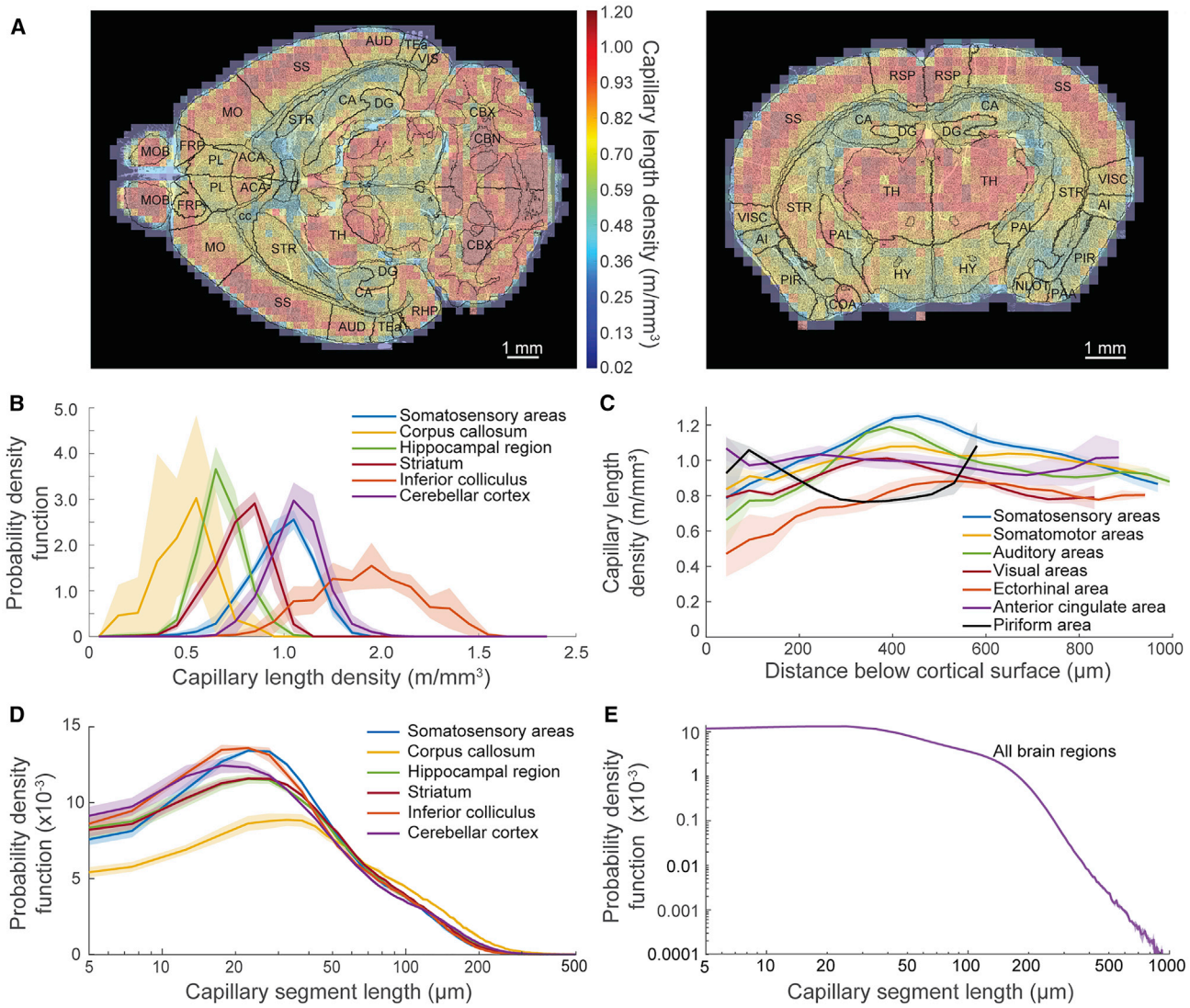


**Figure 5. Descriptive statistics of capillary length**

(A) Local capillary length density overlaid on a 240-μm-thick maximum projections of reconstructed vessels. Full names for the abbreviations are summarized in Table S4.

(B) The PDF of capillary length density of 240-cubes in selected brain regions. Solid lines and transparent shadow show mean and SD for six hemispheres, the same as (D).

(C) The depth dependence of the capillary length density within different regions of neocortex and piriform cortex. Solid lines and transparent shadow show mean and SE for six hemispheres.

(D) The PDF of the length of individual capillary branches within selected brain regions. Regions with higher vessel density have more short vessel segments.

(E) The PDF of the length of individual capillary branches in the entire brain. Solid line and transparent shadow show mean and SD for 3 brains.

told, regions with higher capillary density have more short branches, and vice versa.

## The distance map from locations in the extravascular space to vessels

An important metric to relate angioarchitecture to physiology is the distribution of distances from any point in the parenchyma to the lumen of the nearest vessel (Figures 6A–6F). We consider all vessels in our analysis, as substrates are available from penetrating vessels as well as capillaries (Intaglietta et al., 1996). We quantified the space-filling properties of vascular network by computing the distance map, denoted $d(\mathbf{r})$, between tissue at location $\mathbf{r} = (x, y, z)$ and its nearest vessel wall (Figure 6A). The mean distance between tissue voxels and their nearest vessel voxels, denoted $\overline{d}$ as found by averaging $d(\mathbf{r})$ over each 240-cube, increases from $\overline{d} = 10.0 \pm 0.20$ μm (mean ± SE) in inferior colliculus to 20.2 ± 3.9 μm in corpus callosum (Figure 6B). Thus, locations in a region with a high length density of capillaries lie

Please cite this article in press as: Ji et al., Brain microvasculature has a common topology with local differences in geometry that match metabolic load, Neuron (2021), https://doi.org/10.1016/j.neuron.2021.02.006



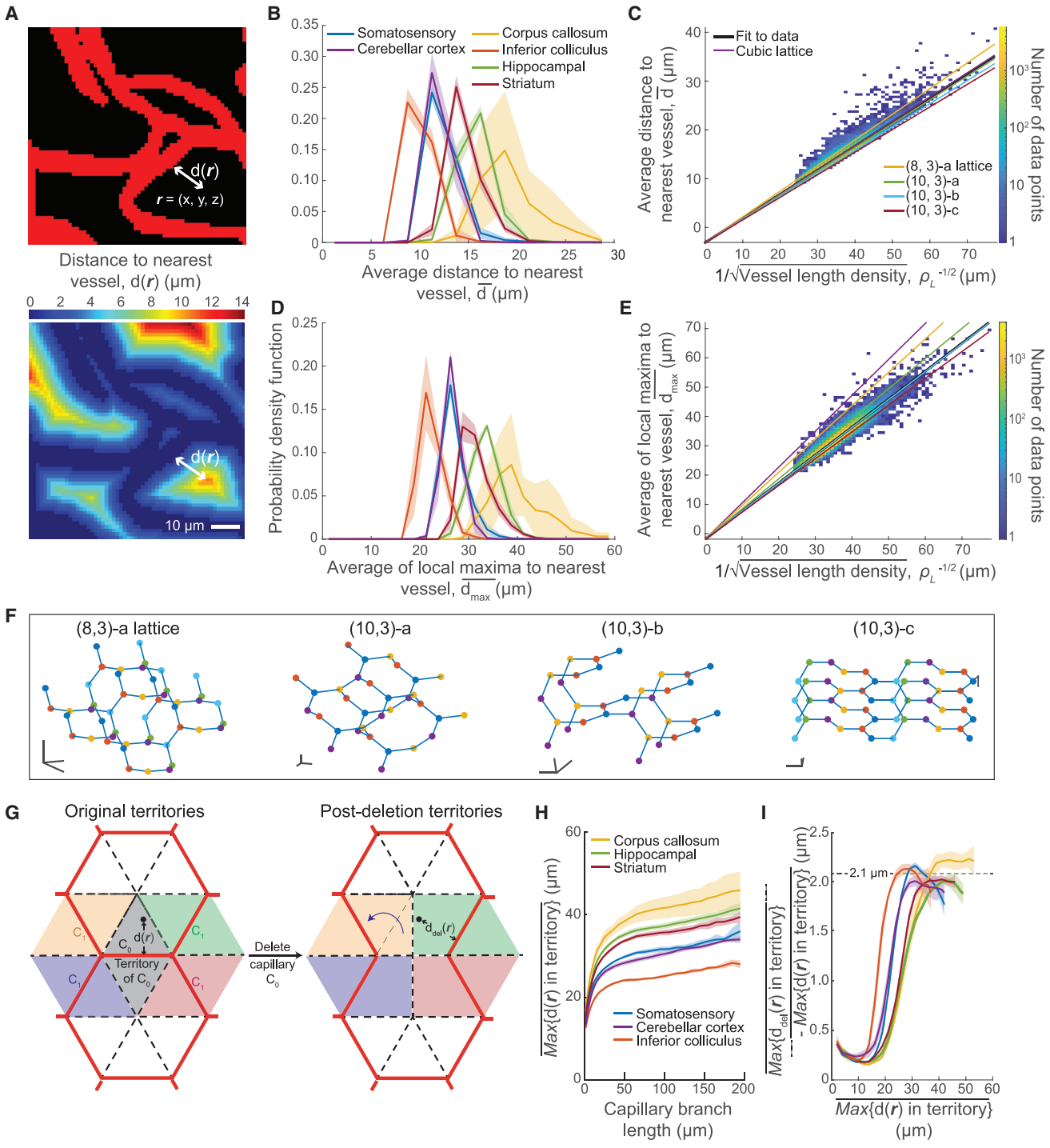


**Figure 6. Scaling relations of space-filling networks**

(A) The distance map, $d(\mathbf{r})$, with respect to vessel segmentation (red). This determines the distance between tissue at **r** and the nearest vessel wall.

(B) The PDF of the average distance between the tissue and the nearest vessel wall in selected brain regions.

(C) Average vessel-tissue distance scales as vessel length density, i.e., $\overline{d} = m\rho_L^{-1/2} - 3.08$ with slope $m = 0.494$; $R^2 = 0.95$. The data encompass 91,751 240-cubes where capillaries accounted for the majority of the vascular volume. Slopes for (8, 3)-a, cubic, (10, 3)-a, (10, 3)-b, and (10, 3)-c lattices are $m = 0.526$, 0.497, 0.487, 0.474, and 0.463, respectively.

(D) The PDF of average tissue-to-vessel distance local maxima $\overline{d_{max}}$ in selected brain regions. Local maxima were found by moving a maximum filter with a window size of 50 μm, which exceeds the fall-off in $\overline{d}$, and averaged over 240-cubes.

*(legend continued on next page)*

Please cite this article in press as: Ji et al., Brain microvasculature has a common topology with local differences in geometry that match metabolic load, Neuron (2021), https://doi.org/10.1016/j.neuron.2021.02.006





relatively close to a vessel (cf. Figures 5B versus 6B), and vice versa.

### Tissue-to-vessel distance scales with vessel length density

We seek a quantitative relation between the distance map and the length density. As scaling laws should depend on the dimensionality but not details of the lattice, we consider first the exact result for a cubic lattice where each branch has the same length. The average distance to the branches between neighboring lattice sites, $\overline{d}$, is related to the length density though $\overline{d} = m\rho_L^{-1/2}$ with slope $m$ = 0.497 (STAR methods). This scaling holds for other three-dimensional, degree-3 lattices (Tran et al., 2013; Figure 6F) with a slope that depends on lattice geometry (Figure 6C). Interestingly, we find that the irregular vascular network, where the irregularity originates from branches that are broadly distributed in length (Figure 5D), tightly follows the scaling relation (Figure 6C). Across all the 240-cubes in which capillaries comprised the major vascular volume (Figure S4), the average tissue-to-vessel distance is proportional to $\rho_L^{-1/2}$ through $\overline{d} = 0.494\rho_L^{-1/2} - 3.08$, where the negative intercept is consistent with vessel radius (Figure 6C). This scaling relation also precisely connects the average tissue-to-vessel distance and length density previously reported for mouse vibrissa somatosensory cortex (Tsai et al., 2009), where $\overline{d}$ = 13.3 ± 1.2 μm and $\rho_L$ = 0.88 ± 0.17 m/mm$^3$.

The vasculature must supply energy substrates to cellular structures that occupy all of the space between vessels. Thus, a physiologically important analysis is to determine the relation between the set of local, maximum distances to each neighboring vessel and the vessel length density across different brain regions. To address this goal, we searched for local maxima in the distance map, denoted $\overline{d_{max}}$, and computed the average value of the local maxima (Figure 6D). The PDF for $\overline{d_{max}}$ across different brain regions yields values that are about twice as large as for the PDF of $\overline{d}$ (Figures 6B and 6D). An exact derivation for a cubic lattice and numerical calculation for regular degree 3 lattices lead to the same scaling law for $\overline{d_{max}}$ as for $\overline{d}$, i.e.,

$$\overline{d_{max}} = n\,\rho_L^{-1/2} - d_0, \qquad \text{(Equation 1)}$$

with slope n = 1.225 for a cubic lattice and n = 0.955 ± 0.001 and $d_0$ = 1.85 ± 0.03 μm for the vascular network (Figure 6E). This analysis provides a quantitative connection between vessel-to-tissue distances and the length density for the irregular vascular networks across all regions of the brain. Given the range of slopes across all degree-3 lattices that we analyzed (Figures 6E and 6F), we suggest that capillary networks might be able to reduce their tissue-to-vessel distance by optimizing the structure of the network while keeping the length density unchanged.

### Consequence of deleting a single capillary

There is a constant background of stalls of red blood cells in a fraction of capillaries (Kleinfeld et al., 1998; Villringer et al., 1994). This increases from about 0.005 of capillaries in normal brains to 0.01–0.02 in mouse models of Alzheimer disease (Cruz Hernández et al., 2019), as well as increases during reperfusion after ischemia (El Amki et al., 2020; Erdener et al., 2021). How does removal of a single capillary impact the distance map? A conceptual illustration that makes use of the distance map shows the territories associated with selected branches (red solid lines in Figure 6G) in a two-dimensional honeycomb lattice. All points in the territory that are closer to the capillary labeled $C_0$ than any other capillary define the territory of $C_0$ (gray area in Figure 6G), with associated distances $d(\mathbf{r})$. We quantify the impact of deleting $C_0$ on expanding the territory of the neighboring vessels by recomputing the shortest distance between $\mathbf{r}$ and the remaining vessels, denoted as $d_{del}(\mathbf{r})$. The territory of $C_0$ is redistributed solely to one of the four capillaries, labeled $C_1$, that were directly connected to $C_0$.

We now estimate the impact of removing an individual capillary for the reconstructed vasculature. The extent of the parenchyma closest to each capillary was parameterized by computing $max\{d(\mathbf{r})\ in\ territory\}$ for each vessel. We found that the average over all capillaries in each of the brain regions, denoted $\overline{max\{d(\mathbf{r})\ in\ territory\}}$, increased as a function of capillary branch length and, further, was greatest for regions with low length density, e.g., corpus callosum, compared to regions with high density (Figure 6H). How sensitive is this distance to loss of a single capillary? The increase in the maximum distance calculated as an average over each region in the brain, i.e., $\overline{max\{d_{del}(\mathbf{r})\ in\ territory\} - max\{d(\mathbf{r})\ in\ territory\}}$, is surprisingly modest (Figure 6I). It is negligible for territories close to a capillary and asymptotes at about 2.1 μm across all brain regions. Thus, while loss of a significant fraction of capillaries lead to a catastrophic loss of connectivity (Figure 6I), deletion of a single capillary appears tolerable, in agreement with the experiment (Nishimura et al., 2006).

(E) Scaling relation between the maximum vessel-to-tissue distance and the vessel length density. Regression for the vascular network was the same in (D), with n = 0.955 and $d_0$ = 1.85 μm; $R^2$ = 0.94. The slope for cubic, (8, 3)-a, (10, 3)-b, (10, 3)-a, and (10, 3)-c regular lattices was n = 1.227, 1.138, 1.027, 0.952, and 0.914, respectively.

(F) Structures of 4 space-filling lattices with 3 nearest-neighbor connections, uniform edge length, and a common branch angle of 120°. The number of branches in the shortest loop for a ($k$, 3) lattice is $k$. Points of the same color in each lattice are related by translation.

(G) Illustration of perturbation analysis for two unit cells of a two dimensional honeycomb capillary lattice (red) before and after removal of one capillary, denoted $C_0$. Capillaries one branch away are denoted $C_1$. The tissue was assigned to the nearest capillary, i.e., gray regions to $C_0$ and color-coded regions to neighboring $C_1$'s. The scalar $d(\mathbf{r})$ is the unperturbed distance map. After deletion of capillary $C_0$, the tissue originally in the territory of $C_0$ was reassigned to the remaining capillaries and the perturbed distance map is $d_{del}(\mathbf{r})$. In this two-dimensional example, the territory of $C_0$ is completely redistributed solely to $C_1$ capillaries, and the maximum distance to a vessel remains unchanged, i.e., $max\{d_{del}(\mathbf{r})\ in\ C_0\ territory\} = max\{d(\mathbf{r})\ in\ C_0\ territory\}$.

(H) The maximum distance between the capillary and the furthest locations in its tissue territory. Solid lines and transparent shadow shown mean and SE as an average over capillary branches in different brain regions, the same as (I).

(I) Increase of the maximum distance between the territory of the deleted capillary and the remaining nearest vessel.

Please cite this article in press as: Ji et al., Brain microvasculature has a common topology with local differences in geometry that match metabolic load, Neuron (2021), https://doi.org/10.1016/j.neuron.2021.02.006



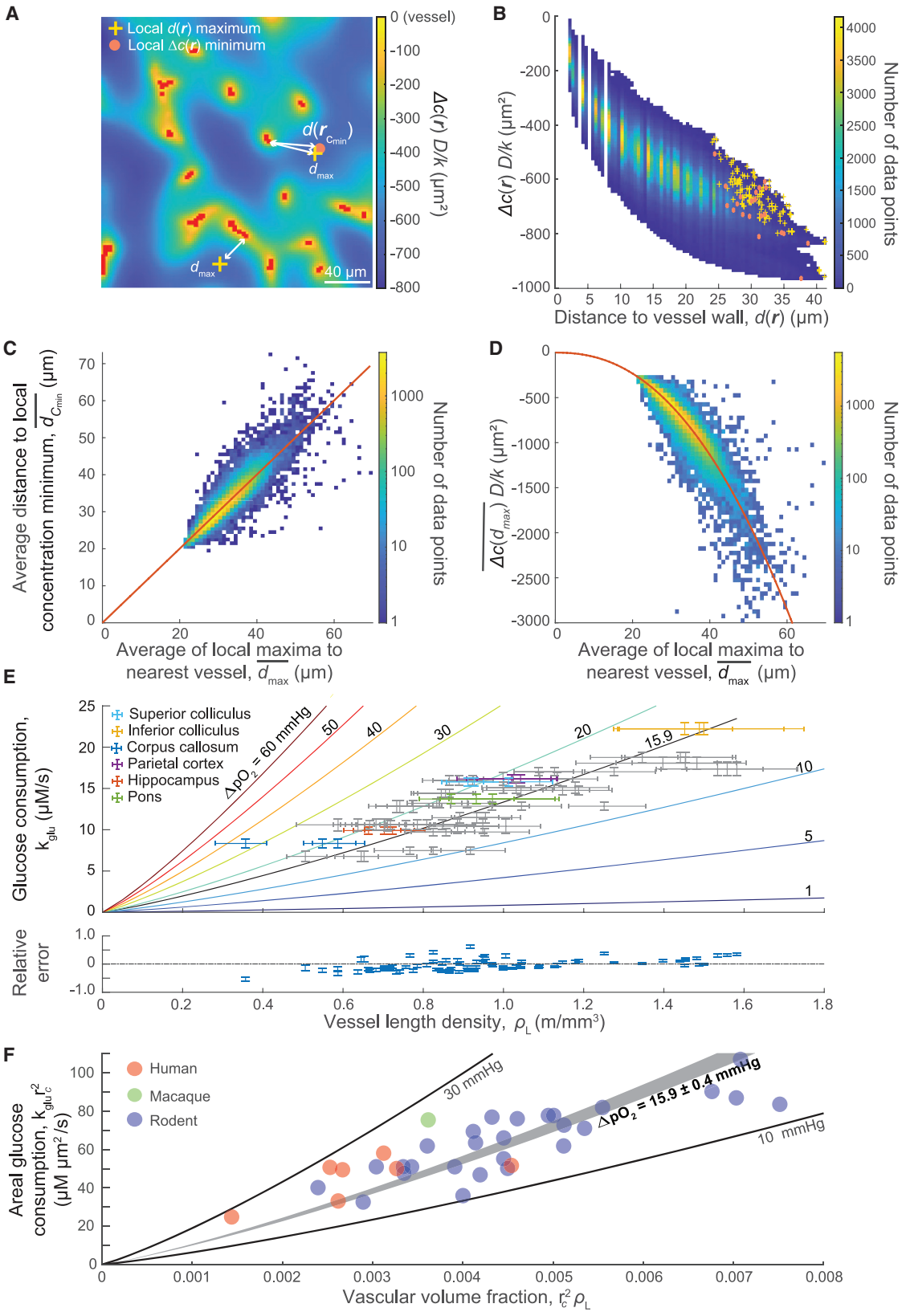


(legend on next page)

Please cite this article in press as: Ji et al., Brain microvasculature has a common topology with local differences in geometry that match metabolic load, Neuron (2021), https://doi.org/10.1016/j.neuron.2021.02.006





### Structural basis of diffusive transport from vessels

Small substrates molecules and metabolites, like $O_2$ and $CO_2$, respectfully, transport between vessels and tissue through diffusion. How does the known heterogeneous metabolism in the brain (Gould and Linninger, 2015; Hawkins et al., 1985; Secomb et al., 2019) relate to network structure? We focus on homeostasis and assume that on the scale of hundreds of micrometers: (1) the metabolism rate and the diffusion coefficient of the substrate of interest are homogeneous throughout the tissue; (2) the concentration of the substrate in the vessel is a constant; and (3) the metabolism rate is independent of substrate concentration. These assumptions allow us to summarize the properties of the substrate with a single parameter, the ratio of the diffusion coefficient, $D$, to the consumption rate, $k$, and model the concentration difference $\Delta c(\mathbf{r})$ between vessel wall and the tissue at $\mathbf{r}=(x,y,z)$ with a Poisson equation (STAR methods). This leads to a three-dimensional map of the change in concentration (example data in Figure 7A) that decreases as one moves away from a vessel until the concentration reaches a minimum where the flux of the substrate goes to zero. We label such points $\Delta c(\mathbf{r}(c_{min}))$ (dot in Figure 7A).

A critical observation is that, under our assumptions, the concentration $\Delta c(\mathbf{r})$ tends to be minimized at the place that the distance $d(\mathbf{r})$ is maximized (cf. black circles and plus signs in Figure 7A and 2D histogram of Figure 7B), i.e., $d(\mathbf{r}(c_{min}))\approx d_{max}$. To examine this correspondence further, we compute the average distance between concentration local minima $\overline{d_{c_{min}}}$ and their nearest vessels and find $\overline{d_{c_{min}}}$ and $\overline{d_{max}}$ to be statistically identical throughout the brain (Figure 7C). This leads to the empirical relation:

$$\overline{d_{c_{min}}} = \overline{d_{max}} \qquad \text{(Equation 2)}$$

that will allow us to connect the average of the concentration minima, denoted $\overline{\Delta c(d_{c_{min}})}$, with $\rho_L$ (Equation 1).

The remaining step is to analytically model the spatial dependence of the concentration minima, i.e., $\overline{\Delta c(d_{c_{min}})}$ (Figure 7D), in a manner that captures the physics of diffusion in the radial direction. We model the data by the radial component of Poisson's equation in cylindrical coordinates and fit a prefactor so that the concentration of substrate at the locations where the flux goes to zero matched the numerical result (Figure 7D). This model accounts for spatial dependence of $\overline{\Delta c(d_{c_{min}})}D/k$, where $D$ is the diffusion constant and $k$ is the rate of consumption, across the entire brain (Figure 7D).

Finally, we apply the model across brain regions where resting state glucose metabolism is known to vary by 3-fold (Hawkins et al., 1985). Under homeostasis, glucose is the main energy source and the glucose consumption rate $k_{glu}$ is related to the oxygen consumption rate $k_{O_2}$ by $\kappa = k_{O_2}/k_{glu} = 5.65$ (Mergenthaler et al., 2013). We combine the scaling laws of Equations 1 and 2 with the solution to Poisson's equation to link the measured quantities $k_{glu}$ and $\rho_L$ in terms of $\Delta pO_2$ (STAR Methods), i.e.,

$$k_{glu} = 4\frac{\alpha_{O_2}D_{O_2}}{\lambda\kappa n^2}\cdot\frac{\rho_L}{\ln\left(n^2/r_c^2\rho_L\right)-1}\cdot\Delta pO_2 \qquad \text{(Equation 3)}$$

where the average capillary radius $r_c$ = 2.19 μm, the prefactor is $\lambda$ = 0.52 (Figure 7D), n = 0.955 (Figure 6F), and we take the limit of $r_c^2\rho_L \ll 1$, i.e., the vasculature occupies a small fraction of the brain. The substrate specific parameters are oxygen diffusion coefficient $D_{O_2}$ = 1.9 μm$^2$/ms and solubility $\alpha_{O_2}$ = 1.3 μM/mmHg (Clark et al., 1978).

How does the scaling of observed glucose metabolism compare with our prediction? We used data measured by [2-$^{14}$C]-glucose utilization in unstressed awake rats across 27 different brain regions (Hawkins et al., 1985). These data span a factor of three in metabolic rate (Table S5). When matched against our measured length density for the same 27 regions (Figure 5), the observed glucose metabolism tracks the length density (Figure 7E). Critically, this relation is described by Equation 3 using a universal drop in oxygen tension, i.e., $\Delta pO_2$ = 15.9 ± 0.3 mmHg (mean ± SE), between the capillary wall and the locations with the lowest $pO_2$ (Figure 7E). For fixed $\Delta pO_2$, the increase of $k_{glu}$ with $\rho_L$ is weakly supralinear for a constant change in oxygen tension. This formula accounts for the known correlation between metabolism rate and vessel length density (Borowsky and Collins, 1989; Weber et al., 2008). It is equally applicable to the diffusive removal of metabolic waste products.

## DISCUSSION

We developed an experimental and computational pipeline to label, image, and reconstruct the microvascular system in whole mouse brains with unprecedented completeness and precision (Figures 1 and 2). Based on our annotated graphs, we identified the brain-wide presence of scale-invariant structural properties.

**Figure 7. Numerical and analytical calculations of substrate diffusion and regional glucose metabolism in terms of vessel length density**

(A) Numerical solution of the change in substrate concentration, $\Delta c(\mathbf{r})$, in one 240-cube. Black circle marks the location of local minimum in concentration $\Delta c(\mathbf{r}(c_{min}))$, while + marks the positions of local maxima in the distance map.

(B) Two-dimensional histogram of the drop in substrate concentration, $\Delta c(\mathbf{r})D/k$, and vessel-to-tissue distance map, $d(\mathbf{r})$. The symbols are defined in (A).

(C) The average distance between tissue local concentration minima and their nearest vessel wall, $\overline{d_{c_{min}}}$, is statistically identical to the value of average tissue-to-vessel distance local maxima, $\overline{d_{max}}$. The slope is 1.00; $R^2$ = 0.88.

(D) Best fit of the solution to the pre-scaled Poisson's equation, $\overline{\Delta c(\mathbf{r})}D/k$, with pre-scaling factor $\lambda$ = 0.52. The fit has $R^2$ = 0.90.

(E) The rate of glucose metabolism versus the vessel length density for different values of $\Delta pO_2$, the drop in $pO_2$ between vessel wall and the minimum $pO_2$ in tissue. The data points are from Hawkins et al. (1985) and seem to maintain a roughly constant drop in $pO_2$. The best fit has $R^2$ = 0.756 and an average absolute relative error of 0.17. Horizontal error bar: median and 25–75 percentiles of regional line density $\rho_L$. Vertical error bar: mean ± SD.

(F) The areal rate of glucose metabolism versus the vascular fraction, corresponding to the vessel length density normalized by the capillary radius, i.e., $r_c^2\rho_L$. We plot average data from three species; data from humans (Cassot et al., 2006; Fernandez-Klett et al., 2020; Hatazawa et al., 1995; Heiss et al., 1984; Ishii et al., 1996; Kubíková et al., 2018; Kuhl et al., 1982; Pantano et al., 1984; Tomasi et al., 2013; Vafaee et al., 2012) and macaque (Kennedy et al., 1978; Weber et al., 2008) are listed in Table S6.

Please cite this article in press as: Ji et al., Brain microvasculature has a common topology with local differences in geometry that match metabolic load, Neuron (2021), https://doi.org/10.1016/j.neuron.2021.02.006



They include the triadic and near-planar structure of nodes (Figures 3A and 3B), the low tortuosity, i.e., relative straightness (Figure 3C), the compact nature of loops of microvessels (Figure 3E), and a near-constant threshold of bond percolation, i.e., the fraction of vessels that can be removed before the network splits apart (Figure 3H). These "design rules" endow the network with a high level of redundancy, such that loss of a single capillary has negligible impact (Figure 6I), as observed (Nishimura et al., 2006), yet lead to a total loss of network function when nearly half of the vessels are lost or have no flow (El Amki et al., 2020; Erdener et al., 2021).

We deduced a simple scaling relation that connects the vessel length density to the vessel-tissue distances for the irregular vascular network across all regions of the brain (Figure 6). We also deduced that the net flux of energy substrates, but not the concentration, delivered by the blood decrements to zero at the locations furthest from the neighboring vessel (Figure 7). This enables us to propose that regional metabolism alters the local vessel density to maintain a constant maximum vessel-to-tissue drop in $pO_2$ (Equation 3), which we verified with literature data for rodent (Figure 7E). This emphasizes the central role of vessel length density as the predominant vasculature structural parameter.

Organ-specific vascular patterns are highly conserved across vertebrates (Larrivée et al., 2009). Thus, our structural findings in rodent brain might generalize to primate vasculatures. There is some limited data on the density of the microvasculature and the metabolic load in different regions of the human brain and in one region of the macaque brain (Table S6). We plot these data and the mouse data on a universal plot where vessel length density is normalized as the vascular fraction $r_c^2 \rho_L$ (Equation 3). While there is unquestioned variability, the data across three species data coalesce in the vicinity of the line for $\Delta pO_2$ = 16 mmHg (Figure 7F). Despite the simplifying assumptions used to develop our model, the observed trend suggests a universal drop in the partial pressure of oxygen throughout mammalian brains.

How realistic is our estimate of $\Delta pO_2 \sim$ 16 mmHg as the largest drop in oxygen tension within tissue in the sedentary mammal (Figures 7E and 7F)? Hypoxic levels of $pO_2$ are taken to be around 10 mmHg (Kasischke et al., 2011), so roughly we require $pO_2 \sim$ 26 mmHg near capillary walls in the sedentary state. This level is well surpassed by the experimentally measured value of $pO_2 \sim$ 40 mmHg near capillary walls (Lyons et al., 2016), with a similar value near penetrating arterioles (Li et al., 2019), in the sedentary state. A more complicated situation occurs during heightened brain activity, where the rate of neuronal metabolism is believed to increase more than 1.9-fold (Bryan et al., 1983), for an estimated increased drop of $\Delta pO_2 \sim 1.9 \times 16 \sim$ 30 mmHg within tissue during heightened brain activity. We now require $pO_2 >$ 40 mmHg near capillary walls in the active state. This can only be achieved by vasodilation and the increase in blood flow associated with the "hemodynamic response" triggered by heightened brain activity (Devor et al., 2011; Zhang et al., 2019).

## Vascular anisotropy

Given the highly organized neural structures revealed by diffusion tensor imaging (Mori and Zhang, 2006) and the shared developmental mechanism of nerve and vessels (Carmeliet and Tessier-Lavigne, 2005), it is not surprising that a large fraction of brain vascular network is nearly anisotropic down to capillary level (Figure 4). These orientation preferences have been described in cortex (Cassot et al., 2006; Kirst et al., 2020) and human white matter (Nonaka et al., 2003), while recent studies have shown the profound impact of cortical vessel anisotropy on magnetic resonance imaging (Báez-Yánez et al., 2017; Gagnon et al., 2015; Hernández-Torres et al., 2017; Viessmann et al., 2019). Our systematic quantification of vessel anisotropy is consistent with past observations in cortex (Cassot et al., 2006; Kirst et al., 2020), provide structural evidence for the orientation-dependent MRI signal in white matter (Hernández-Torres et al., 2017; Viessmann et al., 2019), and reveal strongly orientated vascular network in superior colliculus and pons (Figure 4F).

## Methodological issues

We chose to acquire data with serial section two-photon microscopy to maintain a stable signal-to-noise ratio and near-constant optical resolution with depth (Figure 1). The earliest techniques used counting of individual sections (Boero et al., 1999; Craigie, 1920), which led to surprisingly close estimates of the length density relative to more recent data (Table 1) but was limited to sampling selected regions rather than complete three-dimensional reconstructions. Tissue-clearing techniques and light sheet microscopy have been combined to generate whole mouse brain vasculature images with relatively short data acquisition times (Di Giovanna et al., 2018; Kirst et al., 2020; Lugo-Hernandez et al., 2017; Todorov et al., 2020; Zhang et al., 2018). Yet light sheet microscopy has reduced resolution when the wavefront of the excitation beam passes through expanses of imperfectly cleared tissue. While this arrangement accelerates image acquisition, it can lead to lower signal-to-noise ratios and potential overestimates of vessel diameter (Kirst et al., 2020; Todorov et al., 2020; Table 1). Last, the section-by-section micro-optical sectioning tomography technique (Li et al., 2010) has similar lateral but better axial resolution than two-photon imaging. However, this technique uses negative labeling so the segmentation may be complicated (Wu et al., 2014; Xiong et al., 2017). Beyond segmentation issues, we calculated capillary radii based on optical deconvolution methods (Figures 2A–2E) and comparisons of identified live and labeled vessels (Figure 2F). The combination of precise measurements and principled analysis provided a complete graph for biophysical modeling and the identification of ubiquitous topological invariants (Figures 3E and 3H) and scaling relations (Equations 1, 2, and 3)

Whole-brain vascular reconstructions give insights into microvessels and their role as local supply chains (Table 1). Yet all efforts to date fail to preserve the complete connectivity back to the systemic circulation. This results from both the collapse and close opposition of surface arteries and veins (Blinder et al., 2013) and the embedding of venous sinuses into the foramina (Cai et al., 2019; Herisson et al., 2018). Moving forward will require an *in situ* analysis of the vasculature, a challenge than may be met with all optical histology (Tsai et al., 2003) and/or X-ray tomographic techniques (Dyer et al., 2017; Quintana et al., 2019; Wälchli et al., 2020).

### Relation to Krogh-Erlang model

Over a century ago, August Krogh reported a formula for calculating the maximum oxygen tension between capillaries and muscle cells (Krogh, 1919). The simplicity and validity of the so-called Krogh-Erlang model are rooted in the near uniform orientation and regularity of capillary network in muscles. Today, technical advances allow us to extend quantitative physiological methods to the highly irregular capillary network in the brain. By combining biophysical analysis with numerical results, we transcended the theoretical intractability of irregular capillary networks. The surprisingly accurate scaling relation between tissue-to-vessel length and vascular length (Equation 1; Figure 6E) allowed us to connect the substrate utilization rate to the vessel length density (Equations 2 and 3; Figures 7E and 7F). This explicit dependence of substrate utilization on vascular density was anticipated by Krogh (1919) and others (Borowsky and Collins, 1989; Weber et al., 2008) but would not have been possible without accurate measurements and quantitative analysis.

## STAR★METHODS

Detailed methods are provided in the online version of this paper and include the following:

- KEY RESOURCES TABLE
- RESOURCE AVAILABILITY
  - Lead contact
  - Materials availability
  - Data and code availability
- EXPERIMENTAL MODEL AND SUBJECT DETAILS
- METHOD DETAILS
  - Vascular fluorescent-gel fill based labeling
  - Chronic cranial window preparation
  - Vascular radius calibration imaging
  - Tissue preparation and whole brain imaging
  - Image stitching
  - Computational resources
  - Image segmentation
  - Segmentation to graph
  - Computing vessel centerline position
  - Graph refinement
  - Classify links with single unconnected endpoint
  - Classify short links with low SNR level
  - Purpose and select linkers
  - Super-resolution radius estimation
  - Vessel image profile simulation
  - Radius estimation with a known PSF
  - Radius - PSF joint estimation
- QUANTIFICATION AND STATISTICAL ANALYSIS
  - Sample deformation correction
  - Perfusion labeling quality quantification
  - Registration to Allen mouse brain atlas
  - Reconstruction quality quantification
  - Vascular network features
  - Local vascular network anisotropy
  - Regional bond percolation transition
  - Geometric scaling relations
  - Diffusive substrate transport and consumption
  - Reported statistics

## SUPPLEMENTAL INFORMATION

Supplemental Information can be found online at https://doi.org/10.1016/j.neuron.2021.02.006.

## ACKNOWLEDGMENTS

We thank David Boas, Anna Devor, Christoph Kirst, Marta Koch, Philipp Mächler, Jonathan Polimeni, and Chris Schaffer for useful discussions, Andrew Recknagel for advice on sample preparation, and Kevin Smith for assistance for the computer systems. This work was funded by the National Institutes of Health, USA (grants NS097265, MH111438, and NS108472) and the Mouselight Project of the Howard Hughes Medical Institute. E.B. contributed to this work prior to joining Amazon Web Services.

## AUTHOR CONTRIBUTIONS

D.K. conceived the project; B.F. and H.L. prepared samples; E.B., J.C., R.L., and T.F. acquired and preprocessed the data; X.J. performed data analysis and modeling; and D.K. and X.J. wrote the manuscript with input from B.F. and R.L. D.K. further attended to the myriad of university rules and documents that govern environmental health and safety, including the ethical use of animals as well as the use of chemicals, controlled substances, hazardous substances, and lasers.

## DECLARATION OF INTERESTS

The authors declare no competing interests.

Received: October 20, 2020
Revised: December 9, 2020
Accepted: February 3, 2021
Published: March 2, 2021

## REFERENCES

Attwell, D., and Laughlin, S.B. (2001). An energy budget for signaling in the grey matter of the brain. J. Cereb. Blood Flow Metab. *21*, 1133–1145.

Attwell, D., Buchan, A.M., Charpak, S., Lauritzen, M., MacVicar, B.A., and Newman, E.A. (2010). Glial and neuronal control of brain blood flow. Nature *468*, 232–243.

Báez-Yánez, M.G., Ehses, P., Mirkes, C., Tsai, P.S., Kleinfeld, D., and Scheffler, K. (2017). The impact of vessel size, orientation and intravascular contribution on the neurovascular fingerprint of BOLD bSSFP fMRI. Neuroimage *163*, 13–23.

Bergel, A., Deffieux, T., Demené, C., Tanter, M., and Cohen, I. (2018). Local hippocampal fast gamma rhythms precede brain-wide hyperemic patterns during spontaneous rodent REM sleep. Nat. Commun. *9*, 1–12.

Blinder, P., Tsai, P.S., Kaufhold, J.P., Knutsen, P.M., Suhl, H., and Kleinfeld, D. (2013). The cortical angiome: An interconnected vascular network with noncolumnar patterns of blood flow. Nat. Neurosci. *16*, 889–897.

Boero, J.A., Ascher, J., Arregui, A., Rovainen, C., and Woolsey, T.A. (1999). Increased brain capillaries in chronic hypoxia. J. Appl. Physiol. *86*, 1211–1219.

Borowsky, I.W., and Collins, R.C. (1989). Metabolic anatomy of brain: A comparison of regional capillary density, glucose metabolism, and enzyme activities. J. Comp. Neurol. *288*, 401–413.

Bryan, R.M., Hawkins, R.A., and Mans, A.M. (1983). Cerebral glucose utilization in awake unstressed rats. Am. J. Physiol. *244*, C270–C275.

Buxton, R.B., Griffeth, V.E., Simon, A.B., and Moradi, F. (2014). Variability of the coupling of blood flow and oxygen metabolism responses in the brain: A problem for interpreting BOLD studies but potentially a new window on the underlying neural activity. Front. Neurosci. *8*, 139.

Cai, R., Pan, C., Ghasemigharagoz, A., Todorov, M.I., Förstera, B., Zhao, S., Bhatia, H.S., Parra-Damas, A., Mrowka, L., Theodorou, D., et al. (2019). Panoptic imaging of transparent mice reveals whole-body neuronal projections and skull–meninges connections. Nat. Neurosci. *22*, 317–327.

Carmeliet, P., and Tessier-Lavigne, M. (2005). Common mechanisms of nerve and blood vessel wiring. Nature *436*, 193–200.

Cassot, F., Lauwers, F., Fouard, C., Prohaska, S., and Lauwers-Cances, V. (2006). A novel three-dimensional computer-assisted method for a quantitative study of microvascular networks of the human cerebral cortex. Microcirculation *13*, 1–18.

Clark, D., Erdmann, W., Halsey, J.H., and Strong, E. (1978). Oxygen diffusion, conductivity and solubility coefficients in the microarea of the brain. In Oxygen Transport to Tissue - III, I.A. Silver, ed. (Plenum Press), pp. 697–704.

Craigie, E.H. (1920). On the relative vascularity of various parts of the central nervous system of the albino rat. J. Comp. Neurol. *31*, 429–464.

Cruz Hernández, J.C., Bracko, O., Kersbergen, C.J., Muse, V., Haft-Javaherian, M., Berg, M., Park, L., Vinarcsik, L.K., Ivasyk, I., Rivera, D.A., et al. (2019). Neutrophil adhesion in brain capillaries reduces cortical blood flow and impairs memory function in Alzheimer's disease mouse models. Nat. Neurosci. *22*, 413–420.

Devor, A., Sakadžić, S., Saisan, P.A., Yaseen, M.A., Roussakis, E., Srinivasan, V.J., Vinogradov, S.A., Rosen, B.R., Buxton, R.B., Dale, A.M., et al. (2011). "Overshoot" of O2 is required to maintain baseline tissue oxygenation at locations distal to blood vessels. J. Neurosci. *31*, 13676–13681.

Di, X., Kannurpatti, S.S., Rypma, B., and Biswal, B.B. (2013). Calibrating BOLD fMRI activations with neurovascular and anatomical constraints. Cereb. Cortex *23*, 255–263.

Di Giovanna, A.P., Tibo, A., Silvestri, L., Müllenbroich, M.C., Costantini, I., Allegra Mascaro, A.L., Sacconi, L., Frasconi, P., and Pavone, F.S. (2018). Whole-Brain Vasculature Reconstruction at the Single Capillary Level. Sci. Rep. *8*, 12573.

Dienel, G.A. (2019). Brain glucose metabolism: Integration of energetics with function. Physiol. Rev. *99*, 949–1045.

Drew, P.J., Shih, A.Y., Driscoll, J.D., Knutsen, P.M., Blinder, P., Davalos, D., Akassoglou, K., Tsai, P.S., and Kleinfeld, D. (2010). Chronic optical access through a polished and reinforced thinned skull. Nat. Methods *7*, 981–984.

Dyer, E.L., Gheshlaghi Azar, M., Perich, M.G., Fernandes, H.L., Naufel, S., Miller, L.E., and Körding, K.P. (2017). A cryptography-based approach for movement decoding. Nat. Biomed. Eng. *1*, 967–976.

Economo, M.N., Clack, N.G., Lavis, L.D., Gerfen, C.R., Svoboda, K., Myers, E.W., and Chandrashekar, J. (2016). A platform for brain-wide imaging and reconstruction of individual neurons. eLife *5*, e10566.

El Amki, M., Glück, C., Binder, N., Middleham, W., Wyss, M.T., Weiss, T., Meister, H., Luft, A., Weller, M., Weber, B., and Wegener, S. (2020). Neutrophils Obstructing Brain Capillaries Are a Major Cause of No-Reflow in Ischemic Stroke. Cell Rep. *33*, 108260.

Erdener, E., Tang, J., Kılıç, K., Postnov, D., Giblin, J.T., Kura, S., Chen, I.c.A., Vayisoğlu, T., Sakadžić, S., Schaffer, C.B., et al. (2021). Dynamic capillary stalls in reperfused ischemic penumbra contribute to injury: A hyperacute role for neutrophils in persistent traffic jams. J. Cereb. Blood Flow. Metab. *41*, 236–252.

Fedorov, A., Beichel, R., Kalpathy-Cramer, J., Finet, J., Fillion-Robin, J.C., Pujol, S., Bauer, C., Jennings, D., Fennessy, F., Sonka, M., et al. (2012). 3D Slicer as an image computing platform for the Quantitative Imaging Network. Magn. Reson. Imaging *30*, 1323–1341.

Fernandez-Klett, F., Brandt, L., Fernández-Zapata, C., Abuelnor, B., Middeldorp, J., Sluijs, J.A., Curtis, M., Faull, R., Harris, L.W., Bahn, S., et al. (2020). Denser brain capillary network with preserved pericytes in Alzheimer's disease. Brain Pathol. *30*, 1071–1086.

Fisel, C.R., Ackerman, J.L., Buxton, R.B., Garrido, L., Belliveau, J.W., Rosen, B.R., and Brady, T.J. (1991). MR Contrast Due to Microscopically Heterogeneous Magnetic Susceptibility: Numerical Simulations and Applications to Cerebral Physiology. Magn. Reson. Med. *17*, 336–347.

Frangi, A.F., Niessen, W.J., Vincken, K.L., and Viergever, M.A. (1998). Multiscale vessel enhancement filtering. In Medical Image Computing and Computer-Assisted Intervention, W.M. Wells, A. Colchester, and S. Delp, eds. (Springer), pp. 130–137.

Gagnon, L., Sakadžić, S., Lesage, F., Musacchia, J.J., Lefebvre, X., Fang, Q., Yücel, M.A., Evans, K.C., Mandeville, E.T., Cohen-Adad, J., et al. (2015). Quantifying the microvascular origin of bold-fMRI from first principles with two-photon microscopy and an oxygen-sensitive nanoprobe. J. Neurosci. *35*, 3663–3675.

Gould, I.G., and Linninger, A.A. (2015). Hematocrit distribution and tissue oxygenation in large microcirculatory networks. Microcirculation *22*, 1–18.

Gould, I.G., Tsai, P., Kleinfeld, D., and Linninger, A. (2017). The capillary bed offers the largest hemodynamic resistance to the cortical blood supply. J. Cereb. Blood Flow Metab. *37*, 52–68.

Gross, P.M., Sposito, N.M., Pettersen, S.E., Panton, D.G., and Fenstermacher, J.D. (1987). Topography of capillary density, glucose metabolism, and microvascular function within the rat inferior colliculus. J. Cereb. Blood Flow Metab. *7*, 154–160.

Guibert, R., Fonta, C., Risser, L., and Plouraboué, F. (2012). Coupling and robustness of intra-cortical vascular territories. Neuroimage *62*, 408–417.

Hatazawa, J., Fujita, H., Kanno, I., Satoh, T., Iida, H., Miura, S., Murakami, M., Okudera, T., Inugami, A., Ogawa, T., et al. (1995). Regional cerebral blood flow, blood volume, oxygen extraction fraction, and oxygen utilization rate in normal volunteers measured by the autoradiographic technique and the single breath inhalation method. Ann. Nucl. Med. *9*, 15–21.

Hawkins, R.A., Mans, A.M., Davis, D.W., Vina, J.R., and Hibbard, L.S. (1985). Cerebral glucose use measured with [14C] glucose labeled in the 1, 2, or 6 position. Am. J. Physiol. Cell Physiol. *248*, C170–C176.

Heiss, W.D., Pawlik, G., Herholz, K., Wagner, R., Göldner, H., and Wienhard, K. (1984). Regional kinetic constants and cerebral metabolic rate for glucose in normal human volunteers determined by dynamic positron emission tomography of [18F]-2-fluoro-2-deoxy-D-glucose. J. Cereb. Blood Flow Metab. *4*, 212–223.

Herisson, F., Frodermann, V., Courties, G., Rohde, D., Sun, Y., Vandoorne, K., Wojtkiewicz, G.R., Masson, G.S., Vinegoni, C., Kim, J., et al. (2018). Direct vascular channels connect skull bone marrow and the brain surface enabling myeloid cell migration. Nat. Neurosci. *21*, 1209–1217.

Hernández-Torres, E., Kassner, N., Forkert, N.D., Wei, L., Wiggermann, V., Daemen, M., Machan, L., Traboulsee, A., Li, D., and Rauscher, A. (2017). Anisotropic cerebral vascular architecture causes orientation dependency in cerebral blood flow and volume measured with dynamic susceptibility contrast magnetic resonance imaging. J. Cereb. Blood Flow Metab. *37*, 1108–1119.

Hudetz, A.G. (1993). Percolation phenomenon: The effect of capillary network rarefaction. Microvasc. Res. *45*, 1–10.

Iadecola, C. (2004). Neurovascular regulation in the normal brain and in Alzheimer's disease. Nat. Rev. Neurosci. *5*, 347–360.

Intaglietta, M., Johnson, P.C., and Winslow, R.M. (1996). Microvascular and tissue oxygen distribution. Cardiovasc Res. *32*, 632–643.

Ishii, K., Sasaki, M., Kitagaki, H., Sakamoto, S., Yamaji, S., and Maeda, K. (1996). Regional difference in cerebral blood flow and oxidative metabolism in human cortex. J. Nucl. Med. *37*, 1086–1088.

Kasischke, K.A., Lambert, E.M., Panepento, B., Sun, A., Gelbard, H.A., Burgess, R.W., Foster, T.H., and Nedergaard, M. (2011). Two-photon NADH imaging exposes boundaries of oxygen diffusion in cortical vascular supply regions. J. Cereb. Blood Flow Metab. *31*, 68–81.

Kaufhold, J.P., Tsai, P.S., Blinder, P., and Kleinfeld, D. (2012). Vectorization of optically sectioned brain microvasculature: Learning aids completion of vascular graphs by connecting gaps and deleting open-ended segments. Med. Image Anal. *16*, 1241–1258.

Kennedy, C., Sakurada, O., Shinohara, M., Jehle, J., and Sokoloff, L. (1978). Local cerebral glucose utilization in the normal conscious macaque monkey. Ann. Neurol. *4*, 293–301.

Kirst, C., Skriabine, S., Vieites-Prado, A., Topilko, T., Bertin, P., Gerschenfeld, G., Verny, F., Topilko, P., Michalski, N., Tessier-Lavigne, M., and Renier, N. (2020). Mapping the Fine-Scale Organization and Plasticity of the Brain Vasculature. Cell *180*, 780–795.

Kleinfeld, D., Mitra, P.P., Helmchen, F., and Denk, W. (1998). Fluctuations and stimulus-induced changes in blood flow observed in individual capillaries in layers 2 through 4 of rat neocortex. Proc. Natl. Acad. Sci. USA *95*, 15741–15746.

Kleinfeld, D., Blinder, P., Drew, P.J., Driscoll, J.D., Muller, A., Tsai, P.S., and Shih, A.Y. (2011). A guide to delineate the logic of neurovascular signaling in the brain. Front. Neuroenergetics *3*, 1.

Krogh, A. (1919). The number and distribution of capillaries in muscles with calculations of the oxygen pressure head necessary for supplying the tissue. J. Physiol. *52*, 409–415.

Kubíková, T., Kochová, P., Tomášek, P., Witter, K., and Tonar, Z. (2018). Numerical and length densities of microvessels in the human brain: Correlation with preferential orientation of microvessels in the cerebral cortex, subcortical grey matter and white matter, pons and cerebellum. J. Chem. Neuroanat. *88*, 22–32.

Kuhl, D.E., Metter, E.J., Riege, W.H., and Phelps, M.E. (1982). Effects of human aging on patterns of local cerebral glucose utilization determined by the [18F] fluorodeoxyglucose method. J. Cereb. Blood Flow Metab. *2*, 163–171.

Larrivée, B., Freitas, C., Suchting, S., Brunet, I., and Eichmann, A. (2009). Guidance of vascular development: Lessons from the nervous system. Circ Res. *104*, 428–441.

Lee, T.C., and Kashyap, R.L. (1994). Building Skeleton Models via 3-D Medial Surface/Axis Thinning Algorithms. Graph. Models Image Proc. *56*, 462–478.

Lee, S.P., Duong, T.Q., Yang, G., Iadecola, C., and Kim, S.G. (2001). Relative changes of cerebral arterial and venous blood volumes during increased cerebral blood flow: Implications for bold fMRI. Magn. Reson. Med. *45*, 791–800.

Li, A., Gong, H., Zhang, B., Wang, Q., Yan, C., Wu, J., Liu, Q., Zeng, S., and Luo, Q. (2010). Micro-Optical Sectioning Tomography. Science *1404*, 1404–1408.

Li, B., Esipova, T.V., Sencan, I., Kılıç, K., Fu, B., Desjardins, M., Moeini, M., Kura, S., Yaseen, M.A., Lesage, F., et al. (2019). More homogeneous capillary flow and oxygenation in deeper cortical layers correlate with increased oxygen extraction. eLife *8*, 450932.

Liu, R., Li, Z., Marvin, J.S., and Kleinfeld, D. (2019). Direct wavefront sensing enables functional imaging of infragranular axons and spines. Nat. Methods *16*, 615–618.

Lugo-Hernandez, E., Squire, A., Hagemann, N., Brenzel, A., Sardari, M., Schlechter, J., Sanchez-Mendoza, E.H., Gunzer, M., Faissner, A., and Hermann, D.M. (2017). 3D visualization and quantification of microvessels in the whole ischemic mouse brain using solvent-based clearing and light sheet microscopy. J. Cereb. Blood Flow Metab. *37*, 3355–3367.

Lyons, D.G., Parpaleix, A., Roche, M., and Charpak, S. (2016). Mapping oxygen concentration in the awake mouse brain. eLife *5*, 1–16.

Mchedlishvili, G. (1986). Arterial Behavior and Blood Circulation in the Brain. 1st ed. (Consultants Bureau).

Mergenthaler, P., Lindauer, U., Dienel, G.A., and Meisel, A. (2013). Sugar for the brain: The role of glucose in physiological and pathological brain function. Trends Neurosci. *36*, 587–597.

Mori, S., and Zhang, J. (2006). Principles of Diffusion Tensor Imaging and Its Applications to Basic Neuroscience Research. Neuron *51*, 527–539.

Murray, C.D. (1926). The Physiological Principle of Minimum Work: I. The Vascular System and the Cost of Blood Volume. Proc. Natl. Acad. Sci. USA *12*, 207–214.

Myronenko, A., and Song, X. (2010). Point set registration: Coherent point drifts. IEEE Trans. Pattern Anal. Mach. Intell. *32*, 2262–2275.

Newman, M. (2010). Networks: An Introduction (Oxford University Press).

Nishimura, N., Schaffer, C.B., Friedman, B., Tsai, P.S., Lyden, P.D., and Kleinfeld, D. (2006). Targeted insult to subsurface cortical blood vessels using ultrashort laser pulses: Three models of stroke. Nat. Methods *3*, 99–108.

Nonaka, H., Akima, M., Hatori, T., Nagayama, T., Zhang, Z., and Ihara, F. (2003). Microvasculature of the human cerebral white matter: Arteries of the deep white matter. Neuropathology *23*, 111–118.

Ogawa, S., Menon, R.S., Tank, D.W., Kim, S.G., Merkle, H., Ellermann, J.M., and Ugurbil, K. (1993). Functional brain mapping by blood oxygenation level-dependent contrast magnetic resonance imaging. A comparison of signal characteristics with a biophysical model. Biophys. J. *64*, 803–812.

Pantano, P., Baron, J.C., Lebrun-Grandié, P., Duquesnoy, N., Bousser, M.G., and Comar, D. (1984). Regional cerebral blood flow and oxygen consumption in human aging. Stroke *15*, 635–641.

Quintana, D.D., Lewis, S.E., Anantula, Y., Garcia, J.A., Sarkar, S.N., Cavendish, J.Z., Brown, C.M., and Simpkins, J.W. (2019). The cerebral angiome: High resolution MicroCT imaging of the whole brain cerebrovasculature in female and male mice. Neuroimage *202*, 116109.

Reichold, J., Stampanoni, M., Lena Keller, A., Buck, A., Jenny, P., and Weber, B. (2009). Vascular graph model to simulate the cerebral blood flow in realistic vascular networks. J. Cereb. Blood Flow Metab. *29*, 1429–1443.

Schmid, F., Tsai, P.S., Kleinfeld, D., Jenny, P., and Weber, B. (2017). Depth-dependent flow and pressure characteristics in cortical microvascular networks. PLoS Comput. Biol. Published online February 14, 2017. https://doi.org/10.1371/journal.pcbi.1005392.

Schmid, F., Barrett, M.J., Jenny, P., and Weber, B. (2019). Vascular density and distribution in neocortex. Neuroimage *197*, 792–805.

Secomb, T.W., Hsu, R., and Pries, A.R. (1998). A model for red blood cell motion in glycocalyx-lined capillaries. Am. J. Physiol. Heart Circ. Physiol. *274*, H1016–H1022.

Secomb, T.W., Bullock, K.V., Boas, D.A., and Sakadžić, S. (2019). The mass transfer coefficient for oxygen transport from blood to tissue in cerebral cortex. J. Cereb. Blood Flow Metab. *40*, 1634–1646.

Shih, A.Y., Rühlmann, C., Blinder, P., Devor, A., Drew, P.J., Friedman, B., Knutsen, P.M., Lyden, P.D., Matéo, C., Mellander, L., et al. (2015). Robust and fragile aspects of cortical blood flow in relation to the underlying angioarchitecture. Microcirculation *22*, 204–218.

Smith, O.K. (1961). Eigenvalues of a symmetric 3 x 3 matrix. Commun. ACM *4*, 168.

Todorov, M.I., Paetzold, J.C., Schoppe, O., Tetteh, G., Shit, S., Efremov, V., Todorov-Völgyi, K., Düring, M., Dichgans, M., Piraud, M., et al. (2020). Machine learning analysis of whole mouse brain vasculature. Nat. Methods *17*, 442–449.

Tomasi, D., Wang, G.J., and Volkow, N.D. (2013). Energetic cost of brain functional connectivity. Proc. Natl. Acad. Sci. USA *110*, 13642–13647.

Tran, J., Yoo, T., Stahlheber, S., and Small, A. (2013). Percolation thresholds on three-dimensional lattices with three nearest neighbors. J. Stat. Mech. *2013*, P05014.

Tsai, P.S., Friedman, B., Ifarraguerri, A.I., Thompson, B.D., Lev-Ram, V., Schaffer, C.B., Xiong, Q., Tsien, R.Y., Squier, J.A., and Kleinfeld, D. (2003). All-optical histology using ultrashort laser pulses. Neuron *39*, 27–41.

Tsai, P.S., Kaufhold, J.P., Blinder, P., Friedman, B., Drew, P.J., Karten, H.J., Lyden, P.D., and Kleinfeld, D. (2009). Correlations of neuronal and microvascular densities in murine cortex revealed by direct counting and colocalization of nuclei and vessels. J. Neurosci. *29*, 14553–14570.

Turner, K.L., Gheres, K.W., Proctor, E.A., and Drew, P.J. (2020). Neurovascular coupling and bilateral connectivity during nrem and rem sleep. eLife *9*, 1.

Vafaee, M.S., Vang, K., Bergersen, L.H., and Gjedde, A. (2012). Oxygen consumption and blood flow coupling in human motor cortex during intense finger tapping: Implication for a role of lactate. J. Cereb. Blood Flow Metab. *32*, 1859–1868.

Viessmann, O., Scheffler, K., Bianciardi, M., Wald, L.L., and Polimeni, J.R. (2019). Dependence of resting-state fMRI fluctuation amplitudes on cerebral

cortical orientation relative to the direction of B0 and anatomical axes. Neuroimage *196*, 337–350.

Villringer, A., Them, A., Lindauer, U., Einhäupl, K., and Dirnagl, U. (1994). Capillary perfusion of the rat brain cortex: An in vivo confocal microscopy study. Circ. Res. *75*, 55–62.

Vyssotsky, V.A., Gordon, S.B., Frisch, H.L., and Hammersley, J.M. (1961). Critical percolation probabilities (bond problem). Phys. Rev. *123*, 1566–1567.

Wälchli, T., Bisschop, J., Miettinen, A., Ulmann-Schuler, A., Hintermüller, C., Meyer, E.P., Krucker, T., Wälchli, R., Monnier, P., Carmeliet, P., et al. (2020). Hierarchical imaging and computational analysis of three-dimensional vascular network architecture in the entire postnatal and adult mouse brain. bioRxiv. https://doi.org/10.1101/2020.10.19.344903.

Wang, Q., Ding, S.L., Li, Y., Royall, J., Feng, D., Lesnar, P., Graddis, N., Naeemi, M., Facer, B., Ho, A., et al. (2020). The Allen Mouse Brain Common Coordinate Framework: A 3D Reference Atlas. Cell *181*, 936–953.

Weber, B., Keller, A.L., Reichold, J., and Logothetis, N.K. (2008). The microvascular system of the striate and extrastriate visual cortex of the macaque. Cereb. Cortex *18*, 2318–2330.

Winnubst, J., Bas, E., Ferreira, T.A., Wu, Z., Economo, M.N., Edson, P., Arthur, B.J., Bruns, C., Rokicki, K., Schauder, D., et al. (2019). Reconstruction of 1,000 Projection Neurons Reveals New Cell Types and Organization of Long-Range Connectivity in the Mouse Brain. Cell *179*, 268–281.

Wu, J., He, Y., Yang, Z., Guo, C., Luo, Q., Zhou, W., Chen, S., Li, A., Xiong, B., Jiang, T., and Gong, H. (2014). 3D BrainCV: Simultaneous visualization and analysis of cells and capillaries in a whole mouse brain with one-micron voxel resolution. Neuroimage *87*, 199–208.

Xiong, B., Li, A., Lou, Y., Chen, S., Long, B., Peng, J., Yang, Z., Xu, T., Yang, X., Li, X., et al. (2017). Precise cerebral vascular atlas in stereotaxic coordinates of whole mouse brain. Front. Neuroanat. *11*, 128.

Yushkevich, P.A., Piven, J., Hazlett, H.C., Smith, R.G., Ho, S., Gee, J.C., and Gerig, G. (2006). User-guided 3D active contour segmentation of anatomical structures: Significantly improved efficiency and reliability. Neuroimage *31*, 1116–1128.

Zhang, L.Y., Lin, P., Pan, J., Ma, Y., Wei, Z., Jiang, L., Wang, L., Song, Y., Wang, Y., Zhang, Z., et al. (2018). CLARITY for high-resolution imaging and quantification of vasculature in the whole mouse brain. Aging Dis. *9*, 262–272.

Zhang, Q., Roche, M., Gheres, K.W., Chaigneau, E., Kedarasetti, R.T., Haselden, W.D., Charpak, S., and Drew, P.J. (2019). Cerebral oxygenation during locomotion is modulated by respiration. Nat. Commun. *10*.

Please cite this article in press as: Ji et al., Brain microvasculature has a common topology with local differences in geometry that match metabolic load, Neuron (2021), https://doi.org/10.1016/j.neuron.2021.02.006





## STAR★METHODS

### KEY RESOURCES TABLE

| REAGENT OR RESOURCE | SOURCE | IDENTIFIER |
|---|---|---|
| Chemicals, Peptides, and Recombinant Proteins | | |
| Isoflurane Solution | Covetrus | CAT#: 1169567761 |
| Fatal-Plus Solution | Vortech Pharmaceuticals, LTD. | NDC: 0298-9373-68 |
| Sodium Chloride | Fisher Chemical | CAT#: S271-500 |
| Potassium Chloride | Fisher Chemical | CAT#: P217-500 |
| Calcium Chloride Dihydrate | Fisher Chemical | CAT#: C79-500 |
| Magnesium Sulfate Heptahydrate | EMD Millipore | CAT#: MX0070-1 |
| Sodium Bicarbonate | Fisher Chemical | CAT#: S233-500 |
| Sodium Carbonate | Fisher Chemical | CAT#: 60-019-81 |
| D-(+)-Glucose | Sigma Aldrich | CAT#: G8270-1KG |
| Heparin Sodium Injection, USP $10{,}000_{\text{USP units}}$/10mL | Sagent Pharmaceuticals | NDC:25021-400-10 |
| Sodium Hydroxide Solution (1N) | Fisher Scientific | CAT#: SS266-1 |
| Gelatin from porcine skin, Type A | Sigma Aldrich | CAT#: G1890-500G |
| Sodium Azide | Sigma Aldrich | CAT#: SX0299-1 |
| Phosphate Buffered Saline | Sigma Aldrich | CAT#: 3813-10PAK |
| Albumin-fluorescein isothiocyanate conjugate | Sigma Aldrich | CAT#: A9771-1G |
| Paraformaldehyde, EM Grade, Purified Granular | Electron Microscopy Sciences | CAT#: 19208 |
| Fluorescein isothiocyanate-dextran | Sigma Aldrich | CAT#: 52471-1G |
| Buprenorphine hydrochloride injection | Par Pharmaceutical | NDC: 42023-179-05 |
| Cyanoacrylate glue | Loctite | No. 401 |
| C&B Metabond | Parkell | S380 |
| Dental acrylic | Lang Dental | CAT#: 1323CLR |
| Experimental models: organisms/strains | | |
| Mouse: C57BL/6J | The Jackson Laboratory | JAX: 000664 |
| Software and algorithms | | |
| 3D Slicer | Fedorov et al., 2012 | https://www.slicer.org/ |
| MouseLight Computation Pipeline | Winnubst et al., 2019 | https://github.com/MouseLightProject/ |
| ITK-SNAP | Yushkevich et al., 2006 | http://www.itksnap.org/pmwiki/pmwiki.php |
| Brain vascular network reconstruction and analysis pipeline | This study | neurophysics.ucsd.edu/software.php |

### RESOURCE AVAILABILITY

#### Lead contact

Further information and requests for resources and reagents should be directed to and will be fulfilled by the Lead Contact, David Kleinfeld (dk@physics.ucsd.edu)

#### Materials availability

This study did not generate new unique reagents.

Please cite this article in press as: Ji et al., Brain microvasculature has a common topology with local differences in geometry that match metabolic load, Neuron (2021), https://doi.org/10.1016/j.neuron.2021.02.006



## Data and code availability

The data supporting the current study have not been deposited in a public repository because of the size (200 TB). These data are available from the corresponding author on request. The source code is available at https://neurophysics.ucsd.edu/software.php and in the Methods S1.

## EXPERIMENTAL MODEL AND SUBJECT DETAILS

3 male C57BL/6 mice between 50-80 days of age contribute to this study. All experimental procedures followed the Guide for the Care and Use of Laboratory Animals and has been approved by the Institutional Animal Care and Use Committee at the University of California, San Diego.

## METHOD DETAILS

### Vascular fluorescent-gel fill based labeling

Adult male mice between 50-80 days of age were prepared for whole brain vascular labeling. Mice were injected ip with heparin (200U) and then overdosed with isofluorane delivered in oxygen and injected with fatal plus (ip injection). For mouse 1 and mouse 2, exsanguination was performed by transcardial perfusion of 60-150 mls Oxygenated Ringers Carbicarb (37°C) with 10U/ml of heparin added to the perfusate. Ringer's perfusate was delivered from a peristaltic pump, set at a pump rate of 30 ml/minute, through a blunted 18 g cannula that was inserted through an incision made in the left ventricle; the right atria was snipped to provide an exit for exsanguinated blood. For mouse 3, exsanguination was performed at a pump rate of 13 ml/minute. Exsangination was judged complete by blood clearing of sternal vessels and of the dental pulp. Following the exsanguination step, the head of the mouse was tilted down; the descending aorta was clamped for mouse 3. Fluorescently labeled gelatin (10% porcine gelatin- 0.4% FITC-BSA in PBS-azide) was then administered from a glass syringe-tubing assembly connected to a blunted perfusion cannula that was inserted into the original incision in the left ventricle. Toward the end of the perfusion, as the perfusion cannula was withdrawn from the left ventricle, a small chip of dry ice was used to rapidly freeze the heart to minimize leakage of the warm gelatin through the perfusion incisions. The entire body was then covered with wet ice for 1 hour to cool the intravascular gelatin. The brain was immersion fixed in the skull by placement in cold paraformaldehyde/PBS for 48 h. After a cold PBS wash step (48 h), the brain was removed from the skull under a fluorescent dissection microscope. The extracted brain was stored in cold PBS.

Gelatin solution was prepared by first blooming the porcine gelatin powder with cold PBS and then microwave heating it to temperatures that were not in excess of 60°C. FITC-BSA in PBS-azide was added to liquefied gelatin that had been cooled to 37°C. While the resultant solution is typically clear after coarse filtration, microscopic examination of the fluorescent gelatin revealed bubbles and occasional particulates. To minimize these defects, the liquefied gelatin was sterile filtered after warming in a 47°C water bath. Residual air bubbles were then removed by suction of the surface after centrifugation (3000 g – 2 min). The filtered labeled gelatin was held in a 47°C water bath and transferred to the warmed glass syringe-tubing assembly just before use.

### Chronic cranial window preparation

Adult (more than 12 weeks old) male wild-type mice (C57BL/6J) were anesthetized with isoflurane using a vaporizer (Ohmeda, Isotec 4), 3% (v/v) in oxygen for induction and 1 - 2% (v/v) for maintenance. Body temperature was maintained at 37°C by a heating pad with feedback control during anesthesia. The animal was given analgesic buprenorphine (s.c., 0.1 μg per g body weight) and placed in a stereotaxic frame. The scalp, the periosteum on the parietal and occipital plates was removed. A 3-mm diameter craniotomy was made over the right somatosensory cortex with the centroid at 1.5 mm posterior to Bregma and 2.5 mm lateral from midline. Dura was left intact. A single piece of 3-mm round coverslip (no. 1, 170-μm thick) was then embedded in the craniotomy and sealed around the edge with cyanoacrylate glue (Loctite, no. 401). Meta-bond (Parkell) was further applied around the edge of the coverslip to reinforce stability. A titanium headbar was glued onto the skull with Meta-bond (Parkell) for head-fixation during *in vivo* imaging. The remaining exposed bone were covered with dental acrylic (Lang Dental) to ensure stability. All experimental procedures on our animals were accordance with Guide for the Care and Use of Laboratory Animals and have been approved by Institutional Animal Care and Use Committee at University of California, San Diego.

### Vascular radius calibration imaging

Imaging was performed 7 days after the cranial window surgery. Habituation training to head fixation was performed for one hour daily for 3 days prior to imaging. A 5% (w/v) solution in physiological saline of fluorescein isothiocyanate-dextran (2 MDa; Sigma no. 52471) was prepared for vascular labeling. Before imaging, mice were briefly anesthetized with isoflurane to label the lumen of blood vessels via a retro-orbital intravenous injection of 50 μL fluorescein isothiocyanate-dextran solution. The cranial window was carefully aligned to be perpendicular to the objective axis using a goniometer stage (Thorlabs, GNL20). Mice stayed awake during imaging.

*In vivo* vascular imaging was performed under a previously developed two-photon microscope (Liu et al., 2019) with Galvo x replaced by a resonant scanner (Cambridge Technology, CRS 8 kHz). The Galvo y (Cambridge Technology, 5-mm mirror 6215H) remained the same. A tunable femtosecond laser (Coherent, Chameleon Discovery) was set to 920 nm, and the imaging power at post-objective was less than 100 mW in all *in vivo* experiments within 500 μm depth. Vasculatures were imaged at $0.2\times0.2\times0.94\ \mu m^3$

through a 25x objective (Olympus, XLPLN25XSVMP2, 25X, 1.0 NA and 4-mm working distance), with system-level aberration correction. The microscope was controlled by ScanImage (Vidrio Technologies) running on MATLAB (Mathworks).

After the mice were perfused with fluorescent-gel, the brain was left intact and remained inside the skull. A repeat imaging with the same setting was performed through the cranial window at the exact same location on the perfused brain.

### Tissue preparation and whole brain imaging

All three brains were embedded in 12% (w/v) gelatin and fixed in 4% paraformaldehyde for 12 h. Index matching for optical clarity was achieved by immersing the sample in solution of 40% DMSO in 10 mM PB with increasing concentrations of D-Sorbitol (up to 40/60 w/v). In *Brain 2* and *Brain 3*, nuclei were stained with 10 μM NuclearID-Red solution (ENZ-52406, Enzo Life Science, Farmingdale, NY). To improving the signal-to-noise level and optical resolution, *Brain 3* was further delipidated after verifying the compatibility of the sample preparation methods. The processed whole brain samples were imaged using a resonant scanner two-photon microscope. Imaging was performed using a 40x/1.3 NA oil-immersion objective (#440752, Carl Zeiss, Oberkochen, Germany) at 0.3× 0.3× 1.0 $\mu m^3$ voxel resolution. The surface of the sample was automatically detected and divided into partially overlapping image stacks of size 385×450×250 $\mu m^3$. After the 250 μm thick block-face was imaged, the vibratome removed the top 175 μm of the tissue before proceeding to the next iteration of imaging. Overlap between adjacent image stacks is 25 μm in lateral direction and 75 μm in axial direction. Detailed description for the protocol in this section could be found in Economo et al. (2016) and Winnubst et al. (2019).

### Image stitching

Feature-based registration algorithm was applied to stitched the partially overlapping image stacks across the whole brain (Economo et al., 2016; Winnubst et al., 2019). As the scale of vessels spans two orders of magnitude, both capillary skeleton and large vessel edges were used as descriptors for estimating local deformation field. Local adaptive thresholding was used to generate vessel segmentation. Vessel skeleton was obtained by morphological thinning (Lee and Kashyap, 1994), while vessel radius was estimated by 2D Euclidean distance transform within the segmentation. Skeleton voxels in vessel segments longer than 10 $\mu m$ with median radius no greater than 3 $\mu m$ were selected as descriptors. For image tiles that include large vessels, position of vessel wall was computed by canny edge detector. Both skeletons and edge voxels in adjacent image tiles were matched by Coherent Point Drift algorithm (Myronenko and Song, 2010) and the matched descriptors were used for computing the nonrigid transformation that projects the image tiles into an integrated image at 0.25 × 0.25 × 1.0 $\mu m^3$ voxel resolution(Winnubst et al., 2019).

### Computational resources

The image stitching pipeline was deployed on a high-performance cluster described in (Winnubst et al., 2019). The rest of the image processing and analysis pipeline was implemented in MATLAB (2019b) and deployed on a desktop workstation with dual Intel Xeon E5-2687W CPUs (2 sockets, 24 cores), 512 GB RAM, a NVIDIA GeForce GTX 1080Ti GPU and a NVIDIA GeForce RTX 2080 GPU.

### Image segmentation

The integrated image was down sampled to 1 $\mu m$ isotropic voxel size and divided into $(240\ \mu m)^3$ image cubes, each cube has 32 $\mu m$ overlaps with its 6-neighbors (top, bottom, front, back, left, right). For each 240-cube, a 3 × 3 × 3 median filter was applied to reduce the noise before background noise level estimation, contrast stretching and intensity normalization. First, the resulting image cube $I$ was down sampled 8 times by max-pooling to calculate the local intensity maximum $I_{max}$ and the local intensity threshold $I_{th}$ was estimated by

$$I_{th} = \max\{0.35 I_{max},\ I_{bg}\}, \tag{1}$$

where $I_{bg}$ was estimated by the mean and standard deviation of the estimated background voxel intensity. $I_{th}$ was smoothed by a 3D Gaussian filter, up-sampled and used to produce intensity-based vessel mask $M_{int}$. We assumed the original image was not saturated and therefore voxels of intensity greater than half of the maximum bit value were also added to the intensity mask $M_{int}$.

Second, we calculated the maximum response of each image voxel to rod-shaped filters at different orientations. For a rod filter orientated at $(\theta, \phi)$ in spherical coordinate, a 3D filter array was generated by:

$$rod(\mathbf{r}; \theta, \phi) = \mathcal{N} \exp\left[ -\mathbf{r}^T \left(\mathbf{R}(\theta,\phi)^T diag\left(\sigma_X^{-2}, \sigma_Y^{-2}, \sigma_Z^{-2}\right)\mathbf{R}(\theta,\phi)\right)\mathbf{r}\right], \tag{2}$$

where $\mathbf{r} = (x, y, z)$, $diag(\cdot)$ was the diagonal matrix and the rotation matrix $\mathbf{R}(\theta, \phi)$ was defined as:

$$\mathbf{R}(\theta,\phi) = \mathbf{R}_Y(\theta)\mathbf{R}_Z(\phi) = \begin{bmatrix} \cos(\theta) & 0 & \sin(\theta) \\ 0 & 1 & 0 \\ -\sin(\theta) & 0 & \cos(\theta) \end{bmatrix} \begin{bmatrix} \cos(\phi) & \sin(\phi) & 0 \\ -\sin(\phi) & \cos(\phi) & 0 \\ 0 & 0 & 1 \end{bmatrix} \tag{3}$$

To approximate a cylinder, $\sigma_Y$ and $\sigma_Z$ were set be 1 $\mu m$ to match the scale of capillaries, while $\sigma_X$ was set to be three orders of magnitude greater $\sigma_Y$. The length of the cylinder was set to be 7 $\mu m$. Voxels with value smaller than $e^{-1}$ were zeroed and $\mathcal{N}$ was the normalization factor calculated after zeroing. Since 3D Gaussian distribution was centrosymmetric, we generated 36 rod filters of different

Please cite this article in press as: Ji et al., Brain microvasculature has a common topology with local differences in geometry that match metabolic load, Neuron (2021), https://doi.org/10.1016/j.neuron.2021.02.006



orientation that uniformly cover the upper half of the unit sphere. These filters were convoluted with the image using Fast Fourier Transform (FFT) and the maximum response of the correlation value for each voxel was recorded in an array as the enhanced image $I_e$.

$I_e$ was used to compute the Frangi vesselness filter (Frangi et al., 1998) at the scale of $\sigma_s \in \{0.5, 1, 2\}$ $\mu m$. After smoothing $I_e$ with a 3-dimensional isotropic Gaussian kernel $G(0, \sigma_s)$ with standard deviation $\sigma_s$, the $\gamma$-normalized derivatives were computed to form the Hessian matrices. The $(\mu, \nu)$ element of the Hessian matrix for voxel $(i,j,k)$ was given by:

$$H_{\mu,\nu}(i,j,k) = \sigma_s^{\gamma}\left[\frac{\partial^2}{\partial\mu\partial\nu}\right]\widetilde{I_e}(i,j,k;\ \sigma_s) \tag{4}$$

where $\gamma = 1$ and $\tilde{I}_e(i,j,k;\ \sigma_s) = G(0,\sigma_s) * I_e$. As a 3 × 3 real symmetric matrix, the eigenvalues of the Hessian matrix $\lambda_1$, $\lambda_2$, $\lambda_3$ were computed using the analytical formula (Smith, 1961) and sorted in ascending order according to their absolute value $(|\lambda_1| \le |\lambda_2| \le |\lambda_3|)$. The Frangi vesselness response at scale $\sigma_s$ was:

$$\mathcal{V}_{\sigma_s} = \begin{cases} 0 & \lambda_2 > 0 \ \text{or} \ \lambda_3 > 0 \\ \left(1 - e^{-\frac{1}{\alpha}\frac{\lambda_2^2}{\lambda_3^2}}\right) e^{-\frac{1}{\beta}\frac{\lambda_1^2}{|\lambda_2\lambda_3|}} \left(1 - e^{-\frac{\sqrt{\lambda_1^2+\lambda_2^2+\lambda_3^2}}{c}}\right), & \text{otherwise} \end{cases} \tag{5}$$

The vesselness response was repeated for all the scales and the final vesselness response was the maximum response across multiple scales:

$$\mathcal{V}(i,j,k) = \max_{\sigma_s} \mathcal{V}_{\sigma_s}(i,j,k) \tag{6}$$

The vessel mask $M_v$ was produced by thresholding the Frangi vesselness response and combined with the intensity mask $M_{int}$ by a voxel-wise AND operation. The Frangi filter provided a relatively reliable way to recognize the cylindric objects, but failed to detect the branch point due to the more complicated geometry. To improve the connectivity accuracy, adaptive hysteresis thresholding was applied to the region outside of the $M_v$ to add voxels of high local signal-to-noise (SNR) level near the existing mask into $M_v$. Finally, small connected components in the segmentation were removed before the vessel mask in a 240-cube was saved.

### Segmentation to graph

We generated a cubic grid of length 1072 μm out of the grid of 240-cubes. These 1072-cubes contained 5 × 5 × 5 240-cubes, with a 240 $\mu m$ overlap with their 6-neighbors. We computed the vessel centerline in each 1072-cube independently, and saved the centerlines in the included 240-cubes separately. The coordinates of centerline voxels in the overlapping 240-cubes were iteratively updated according to their minimum distance to the boundary of the 1072-cubes. This resulted in a continuous centerline throughout the brain, where the final position of every centerline voxel was at least 240 μm away from the boundary.

### Computing vessel centerline position

For each 1072-cube, the masks in 125 240-cubes were stitched for computing the vessel centerline. First, small holes in the segmentation were filled by morphological operation. The resulting mask was skeletonized by removing the ''removable simple points'' in the mask from 6 directions iteratively. The ''removable simple point'' was defined as the voxel that was not an endpoint (with only one 26-neighbor) and whose removal does not changes the topology of the skeleton (measured by the Euler characteristic) (Lee and Kashyap, 1994). Note that this algorithm only produced a skeleton that approximates the centerline. To refine the position of the skeleton voxels for radius estimation, we assumed that microvessels have the brightest intensity along the centerline and moved the skeleton voxels to their brighter neighbors, if the adjustment did not alter the topology of the skeleton. For each skeleton voxel, we searched for brighter background voxels in its 26-neighboring, among which we selected the brightest one that (1) was a ''removable simple point'' in the original configuration, and (2) made the original skeleton voxel a ''removable simple point'' in its 26-neighbors if it was added to the skeleton. This ''centering'' procedure was carried out iteratively until no skeleton voxel could be moved. Voxels that became ''removable simple points'' were removed along the way of centering. The centerline voxels radii were initialized as the distance between skeleton voxels and the nearest vessel boundary by 3D Euclidean distance transform (DT).

To convert the skeleton to graph, skeleton voxels were classified into endpoint, link, and node voxels according to the number of skeleton voxels in their 26-neighbors. Voxels with more than 2 neighbors were used to construct a mask, from which the connected components (CC) formed the nodes in the graph. The remaining voxels were used to construct another mask, where the connected components formed the edge of the graph. To enable a rapid reconstruction of the graph in whole-brain scale, sparse matrices were used for searching the connected components. A MATLAB structure was designed to store the position and radius of every centerline voxel in the node and edge connected components, as well as the connectivity between nodes and edges.

### Graph refinement

The skeletonization algorithm preserved the topological characteristics of the vessel mask and is highly sensitivity to segmentation errors: a false positive voxel in the segmentation could lead to a false positive connection, while a false negative voxel could lead to an

Please cite this article in press as: Ji et al., Brain microvasculature has a common topology with local differences in geometry that match metabolic load, Neuron (2021), https://doi.org/10.1016/j.neuron.2021.02.006





artificial loop or hole. To improve the graph connectivity accuracy, we developed a classifier-based pipeline to automatically refine the derived vessel graph across the brain.

First, short free-ended links and loops consist of one or two links were deleted. The short free-ended links were mainly artifacts of the skeletonization algorithm, while short loops were the result of stitching artifacts and noise. Among all the possible configurations of loops, a ''self-loops'' is a link that connect a node back to itself, while a ''bi-link loop'' has a pair of links connecting a pair of nodes. Self-loops are not biologically plausible, though ''apparent'' long self-loops could appear when one of the nodes of bi-link loops happen to be on the edge of the 1072-cube. Short bi-link loops were found to be mainly artifacts under visual inspection. As deleting a link changed the identity of the connected links, the graph needed to be iteratively updated during deletion, as described below:

**Algorithm 1:** Delete short free-ended links and short loops

```
needRefinementQ = true;
while needRefinementQ do
    Delete free-ended link of length ≤ 2 μm;
    Find links that connect a node to itself (“self-loop”) and delete the ones
    of length ≤ 30 μm;
    Find loops that consist of two links and at least one of the links of length
    ≤15 μm. For each of these loops, delete its link with lower average
    fluorescence intensity;
    Update the graph;
    if no link deleted then
        needRefinementQ = false;
    end
end
```

### Classify links with single unconnected endpoint

The remaining free-ended links could be artifacts or incompletely labeled vessels. For links with one unconnected endpoint, a random forest classifier was trained to further identify segments for removal using the following features:

- Segment length
- Maximum, minimum, mean, standard deviation and coefficient of variance of the skeleton voxel radii
- Median, coefficient of variance and SNR level of the skeleton voxel intensity
- Intensity difference between the two voxels at the end of the segment
- Ratio between maximum skeleton voxel radius and segment length
- Distance to the nearest unconnected endpoint voxel
- Inner product between the segment tangent vector and the nearest unconnected endpoint tangent vector
- Number of skeleton voxels in the segment of the nearest unconnected endpoint

### Classify short links with low SNR level

The inter-capillary distance could be only a few micrometers, which is comparable to the axial optical resolution. These nearby vessels might be incorrectly connected by the segmentation algorithm. We trained classifiers to reduce this type of false positive connections. First, we selected vessel segments with the following criteria as candidates:

- Minimum skeleton voxel intensity is lower than a threshold (depends on the imaging system and image intensity histogram)
- Segment length $<25\ \mu m$
- Ratio between the sum of endpoints radii and segment end-to-end distance >0.15

Another random forest classifier was trained to identify the false positive connections among the candidates using the following features:

- Segment length and end-to-end distance
- Maximum, minimum, median, standard deviation and coefficient of variance of the skeleton voxel radii
- Minimum, Mean, median, standard deviation and coefficient of variance of the skeleton voxel intensity
- Relative position of the minimum intensity voxel along the segment skeleton, and its normalized distance to the middle
- Intensity of the middle skeleton voxel, intensity different between the middle skeleton and the minimum intensity of the skeleton voxels
- Ratio between the sum of endpoints radii and segment end-to-end distance
- Ratio between the difference in endpoints radii and the segment length
- Ratio between the middle intensity and the maximum intensity of the skeleton voxel
- Ratio between the middle intensity and the maximum intensity at the two ends of the segment

- SNR level of the surrounding vessel mask, segment skeleton, and the middle skeleton voxel
- Difference between average endpoint intensity and the middle skeleton voxel intensity, normalized by the average endpoint intensity
- The z-component of the segment end-to-end unit vector

### Purpose and select linkers

For the remaining free-ended links, a modified version of threshold relaxation algorithm (Kaufhold et al., 2012) was used to propose the possible voxel lists (linkers) that connect the unconnected endpoints to their surrounding skeleton. First, the local volume of vessel image, existing vessel mask and skeleton were cropped around the unconnected endpoint. The cropped vessel image was then thresholded by iteratively decreasing intensity threshold until getting a CC that contained both the unconnected endpoint and voxels in the original vessel mask that are not connected to the unconnected endpoint in the cropped volume. This CC defined the search space for finding the ''linker'' to bridge the endpoint to its neighboring skeleton. Voxels in this search space were used to construct an undirected graph, where each node had intensity-weighted edges connecting to their 6-neighbors in the CC. The Dijkstra's shortest path algorithm was applied to obtain an ordered set of voxel coordinates (denote as a linker) that maximize the SNR level.

For each linker, the following features were computed, and the third random forest classifier was trained to further select the linkers to be added to the existing skeleton.

- Original length of the link with the endpoint
- Number of links in the cropped volume
- Number of adjacent links of the linker
- Linker length, end-to-end distance, straightness, end-to-end vectors of the linker
- Ratio between the length of the linker and the link with the endpoint
- Mean, standard deviation and signal to noise level of the linker voxel intensity
- Mean, standard deviation and signal to noise level of the linker voxel intensity outside the original vessel mask
- Linker radius (derived from the radii of the skeleton voxels near the two ends of the linker)
- Mean, median, standard deviation and SNR level of the voxel intensity in the reconstructed mask of the linker
- Mean and standard deviation of the intensity of the background voxels near the linker mask
- Mean and standard deviation of the ratio between linker-skeleton distance and linker-endpoint distance
- Inner product between the endpoint tangent vector and the linker end-to-end vector
- Number of unconnected endpoints in the link
- Number of times the derivative of the linker voxel - skeleton distance change sign

For a link with one unconnected endpoint, the endpoint voxel might be converted to link voxel if the linker was added, or remain an endpoint voxel if the linker was rejected by the classifier. For a link with two unconnected endpoints, if the linkers for both endpoints were rejected, the link was deleted directly. Otherwise, the link might become part of a new link with 0, 1, or 2 unconnected endpoints. The remaining links with endpoint(s) could be further refined in the next iteration. The entire graph refinement process was repeated 3 times for each 1072-cubes. In summary, the graph refinement process could be abstracted as below:

**Algorithm 2:** Graph refinement

```
i = 0; needRefineQ = true;
while i < 3 & needRefineQ do
  i = i + 1;
  Delete short free-ended links and short loops;
  Find, quantify, and classify links with single endpoint to delete. Update
  graph;
  Find, quantify, and classify short links with low SNR to delete. Update
  graph;
  Find, quantify, and classify linkers to add. Update graph;
  Delete unmodi_ed links with two unconnected endpoints;
  Delete short free-ended links and short loops;
  if graph is not modified then
    needRefineQ = false
  end
end
```

We implemented a MATLAB GUI to facilitate labeling link CCs for training the classifiers. Thousands of link CCs from a few 1072-cubes in different regions of the brain were labeled and randomly split into 80%–20% for training and testing, respectively. The resulting classifiers were used for automatically refining the vessel graph in the whole brain. All classifiers achieved more than 95% accuracy.

Please cite this article in press as: Ji et al., Brain microvasculature has a common topology with local differences in geometry that match metabolic load, Neuron (2021), https://doi.org/10.1016/j.neuron.2021.02.006



CellPress

### Super-resolution radius estimation

We pre-computed the light intensity profiles near vessels of different radius at different orientation. These intensity profiles were used to iteratively estimate the vessels radius and the Point Spread Function (PSF) in selected brain regions, and the resulting averaged PSF was used to estimate vessel radius throughout the brain.

### Vessel image profile simulation

PSF was model as a 3D Gaussian with diagonal covariance matrix $diag(\sigma_{xy}, \sigma_{xy}, \sigma_z)$ with rotational symmetry on x-y plane. Vessel was locally approximated as a cylinder along x-direction, of radius $r$ and elevation angle $\theta$ (with respect to the horizontal plane) with uniform lumen fluorescence density. The 3D theoretical vessel images were computed as the convolution between the cylinder and the PSF. The simulation voxel size was chosen to be less than 20% of the smallest relevant scale ($r$, $\sigma_{xy}$, and $\sigma_z$). For each set of parameters, lateral radial (along $y$-direction) and axial radial (along $z$-direction) intensity profile ($I_{xy}(y|r,\theta,\sigma_{xy},\sigma_z)$ and $I_z(z|r,\theta,\sigma_{xy},\sigma_z)$) were recorded and the normalized edge intensity in the radial direction on horizontal plane was defined as:

$$I_{th}(r,\theta,\sigma_{xy},\sigma_z) = \frac{I_{xy}(r|r,\theta,\sigma_{xy},\sigma_z)}{I_{xy}(0|r,\theta,\sigma_{xy},\sigma_z)}. \quad (7)$$

The simulation was done for series of radius ($r \in [0.5, 15]\ \mu m$), elevation angle ($\theta \in [0, \pi/2]$) and PSF size ($FWHM_{xy} \in [0.45, 2]\ \mu m$ and $FWHM_z \in [1.33, 12]\ \mu m$).

### Radius estimation with a known PSF

Initially, vessel radius $\rho$ was estimated as the distance between skeleton voxel and the nearest voxel not in the vessel mask. Vessel segment local elevation angle $\theta$ was calculated using the coordinates of the neighboring skeleton voxels. Given PSF parameters, radius estimation was refined iteratively in the following way:

**Algorithm 3:** Radius estimation
$r_0 = -1$; n = 1; N = 6;
Initialize radius estimate $r_e$ from vessel segmentation;
Calculate skeleton voxel position $\boldsymbol{x}_s$ in 0:25 μm resolution image stack;
Crop 0:25 μm resolution image stack around $\boldsymbol{x}_s$ according to $r_e$, denote as $I(\boldsymbol{x})$;
Locally search for the intensity maximum $I_{\max}$ around $\boldsymbol{x}_s$;
Estimate background light intensity level $I_{bg}$;
Normalize light intensity: $I_n(\boldsymbol{x}) = \frac{I(\boldsymbol{x}) - I_{bg}}{I_{\max} - I_{bg}}$;
**while** $r_0 \neq r_e$ & n $\leq N$ **do**
  $r_0 = r_e$, $n = n + 1$;
  Use $r_e$ and $\theta$ to calculate normalized edge intensity $I_{th}(r_e, \theta, \sigma_{xy}, \sigma_z)$;
  Generate local vessel segmentation $M(\boldsymbol{x}) = I_n(\boldsymbol{x}) \geq I_{th}$;
  Apply morphological close to $M(\boldsymbol{x})$;
  Compute 2D distance transform $D(\boldsymbol{x})$ for each horizontal plane of $M(\boldsymbol{x})$;
  $r_e$ = Local maximum of $D(\boldsymbol{x})$ around $\boldsymbol{x}_s$;
end
The estimation normally converged within 3 iterations.

### Radius - PSF joint estimation

The radius estimation algorithm mentioned above assumed known PSF inside the tissue, but the actual PSF size in tissue differed from the measurement under ideal imaging conditions. To improve the accuracy of radius estimation, we iteratively estimated both PSF and vessel radius by an additional layer of PSF estimation:

**Algorithm 4:** PSF-Radius Joint Estimation
$\mathcal{L}_{\max} = -1$; $\mathcal{L}_0 = -2$; n = 0; N = 6;
Initialize $\sigma_{xy}$ and $\sigma_z$ by rough estimation from image;
Initialize $r_e$ from vessel segmentation;
**while** $\mathcal{L}_0 < \mathcal{L}_{\max}$ & n < $N$ **do**
  n = $n$ + 1, $\mathcal{L}_0 = \mathcal{L}_{\max}$;
  Calculate skeleton voxel position $\boldsymbol{x}_s = (x_s, y_s, z_s)$ in 0.25 μm resolution image stack; Update $r_e$ using Algorithm 3;
  Get axial intensity profile at: $i_z(z|x_s, y_s)$;
  Get lateral radial intensity profile $i_{xy}(\hat{r}|\phi, z_s)$, where $\phi$ is the azimuth angle of the vessel radial direction, and $\hat{r} = \sqrt{(x - x_s)^2 + (y - y_s)^2}$;
  For all the simulated PSF parameter sets $\{\sum_{xy}, \sum_z\}$, calculate the

Please cite this article in press as: Ji et al., Brain microvasculature has a common topology with local differences in geometry that match metabolic load, Neuron (2021), https://doi.org/10.1016/j.neuron.2021.02.006



angle-weighted normalized cross-correlation C(●, ●) between measured light intensity $i$ and simulated light intensity $I$:

$\mathcal{L}(\sum_{xy}, \sum_z) = \frac{1}{1+\cos(\theta)}\{C(|i_{xy}|(\hat{r}|\phi, z_s), I_{xy}(\hat{r}|r_e, \theta, \sum_{xy}, \sum_z)) + \cos(\theta)C(i_z(z|x_s, y_s), I_z(z|r_e, \theta, \sum_{xy}, \sum_z))\}$;

Update PSF estimation by maximizing $\mathcal{L}$:

$\{\mathcal{L}_{\max}, \sigma_{xy}, \sigma_z\} = \arg\max_{\sum_{xy}, \sum_z} \mathcal{L}(\sum_{xy}, \sum_z)$;

end

## QUANTIFICATION AND STATISTICAL ANALYSIS

### Sample deformation correction

Sample deformation was quantified by comparing the vascular images in different steps of the sample preparation process with the *in vivo* images. In *Brain2*, part of the vasculatures in somatosensory cortex was imaged *in vivo* and right after perfusion before the brain was extracted. The vessel centerlines in post-perfusion images were aligned to the vessel centerline voxels in the *in vivo* images by similarity transformation to quantify the scale changes during perfusion. After whole brain vasculature imaging and reconstruction, the final vessel centerlines were registered to the post-perfusion vessel skeleton by Affine transformation. Sample deformation in three-dimensions was quantify by QR decomposition of the Affine transformation matrix. A very uniform sample shrinkages was found in three orthogonal directions and therefore their geometric average (1.051) was applied to correct the length scales. (Figure S3). To further quantify the stability of the shrinkage, the same sample preparation procedures were applied to the brains used for vascular radius calibration experiments. For ten 180 $\mu m$×180 $\mu m$×400 $\mu m$ volumes in one brain, a linear scaling factor of 1.048 ± 0.007 was found. The extra sample deformation due to the delipidation process applied to *Brain 3* was quantified by registering its whole brain image stack to the whole brain image of *Brain 1* at 16 μm isotropic resolution using similarity transformation in MATLAB. The resulting linear scaling factor of 1.0926 was applied to correct the length scales.

### Perfusion labeling quality quantification

The *in vivo* and post perfusion cortical vascular images used for vessel radius calibration were processed to extract the vessel skeleton. Vessel skeleton was used to compute the similarity transformations from the post perfusion image to the *in vivo* images. The post perfusion images were transformed to overlay on the *in vivo* images according to the similarity transform. To facilitate visual inspection, RGB images were synthesized by using the *in vivo* images as the red channel, the post perfusion images as the blue channel, and the average of the *in vivo* and post perfusion images as the green channel. Moreover, the reconstructed vessel graphs in the post perfusion images were transformed and added to the green channel (of value 255), while the unconnected endpoints were added to the red channel (of value 255). For each channel, 20 μm moving maximum intensity projection was computed and the max-projection images were further enhanced by saturating the grayscale value of 2.5% of the pixels. Classifier-based graph refinement was not applied the extracted vessel skeleton, and therefore the position of the unconnected endpoints helped to highlight the potential unlabeled vessels in the post perfusion image. The unlabeled parts of the vessel segments in the post perfusion images had signal level comparable to its adjacent background. The image stacks were inspected multiple times and any uncertainties in the filling completeness were verified in the original images. 15 regions of size 180×180×400 $\mu m^3$ from 3 mice (5 regions from each) were inspected. Among 2835 inspected vessel segments, 7 were partially unlabeled (Figure S1).

### Registration to Allen mouse brain atlas

Whole brain image stacks were down-sampled to 25 $\mu m$ isotropic resolution and aligned to the Allen mouse common coordinate framework version 3 (CCFv3). The nucleus staining channel of *Brain3* was registered to the average template at 25 $\mu m$ using intensity-based Affine transformation in the BRAINS module of 3D Slicer (https://www.slicer.org/) (Fedorov et al., 2012), and the registration was further refined by iterative landmark thin-plate registration. Registration was saved as deformation field to transform the atlas annotation and the binary hemisphere mask to the image space by nearest-neighbor interpolation. For *Brain1* and *Brain2*, vascular images of *Brain3* were used as anatomical template for both the Affine transformation and landmark registration. The resulting deformation fields were used to transform the registered annotation of *Brain3*.

### Reconstruction quality quantification

To quantify the reconstruction quality of the microvascular network, six 240-cubes were randomly selected from cortical regions, thalamus, superior colliculus and pons to reconstruct the microvascular network and visualized using itk-snap software (Yushkevich et al., 2006) along with the image at 1 μm resolution. To highlight the vessel segments with unconnected endpoints inside the volume, unconnected endpoints voxels that are at least 1 voxel away from the cube edges were reconstructed as spheres and visualized in a separate color (green). Reconstruction errors, including unconnected segments, potential false positive connections due to the proximity of microvessels, sample preparation and image processing, were detected by visually tracing the reconstruction mask overlaid on the image and inspecting the three-dimensional visualization. Among 2133 inspected segments, 1 false positive connection and 2 unconnected segments were founded (Figure S1).

Please cite this article in press as: Ji et al., Brain microvasculature has a common topology with local differences in geometry that match metabolic load, Neuron (2021), https://doi.org/10.1016/j.neuron.2021.02.006



CellPress

## Vascular network features

### Link features

Vessel segment $i$ with $n_i$ skeleton voxels was recorded as an ordered set:

$$E_i = \left\{\mathbf{x}_1^{(i)}, \mathbf{x}_2^{(i)}, \ldots, \mathbf{x}_{n_i}^{(i)}\right\}, \tag{8}$$

where voxel at $\mathbf{x}_j^{(i)}$ was the 26-neighbor of voxels at $\mathbf{x}_{j-1}^{(i)}$ and $\mathbf{x}_{j+1}^{(i)}$. Each skeleton voxel $j$ was associated with a radius and the radius of the vessel segment $r_i$ was defined as the median of its skeleton voxel radii.

- Length: $l_i = 1 + \sum_{j=1}^{n_i-1} \| \mathbf{x}_j^{(i)} - \mathbf{x}_{j+1}^{(i)} \|_2$
- End-to-end vector: $\mathbf{V}_e^{(i)} = \mathbf{x}_{n_i}^{(i)} - \mathbf{x}_1^{(i)}$
- End-to-end distance: $d_{ep}^{(i)} = \| \mathbf{V}_e^{(i)} \|_2 + 1$
- Orientation vector: $\mathbf{v}_e^{(i)} = \mathbf{V}_e^{(i)} / d_{ep}^{(i)}$
- Surface area: $S_i = 2\pi r_i l_i$
- Volume: $V_i = \pi r_i^2 l_i$
- Straightness: $s_i = d_{ep}^{(i)} / l_i$
- Tortuosity: $l_i / d_{ep}^{(i)}$
- Tangent vector at endpoint $\mathbf{x}_1^{(i)}$ ($\mathbf{x}_{n_i}^{(i)}$): $\mathbf{v}_{t,1}^{(i)}$ ($\mathbf{v}_{t,2}^{(i)}$) was the leading principal component of the 3D coordinate of the first (last) 10 (or $n_i$) skeleton voxels in the vessel segment $i$, with negative (positive) inner product with the orientation vector $\mathbf{v}_e^{(i)}$ ($\mathbf{v}_e^{(i)} \cdot \mathbf{v}_{t,1}^{(i)} < 0$, $\mathbf{v}_e^{(i)} \cdot \mathbf{v}_{t,2}^{(i)} > 0$).
- Is capillary: $Q_i$ equals 1 if the link has radius $r_i$ no greater than $r_{cap} = 3.5\mu m$ and 0 otherwise.
- Capillary branch order: geodesic distance to the nearest non-capillary. Starting from noncapillaries, the vessel segments directly connect to the noncapillaries are defined as capillaries of branch order 1. The unlabeled capillaries directly connect to the branch order 1 capillaries are defined as branch order 2. The labeling continues until no capillary segments can be labeled.
- Number of edges in the shortest loop: number of vessel segments in the shortest loop measured by segment length

Distance transform with respect to the reconstructed vessel mask gave the distance transform field $d(\mathbf{x})$ whose value at $\mathbf{x}$ was the minimum distance between the tissue at $\mathbf{x}$ and the nearest reconstructed vessel wall. In single vessel segment removal perturbation analysis, denote the distance between tissue at $\mathbf{x}$ and its nearest vessel after perturbation as $d_p(\mathbf{x})$. For vessel segment $i$, the voxels in the tissue whose distance to segment $i$ was smaller than to any other segments were defined to be in the tissue territory $t_i$ of segment $i$.

- Maximum distance to the territory tissue: $d_{max}^{(i)} = Max\{d(\mathbf{x}) \text{ interritory}\} = \max_{\mathbf{x}\in t_i}\{\mathrm{d}(\mathbf{x})\}$
- Maximum distance between the territory tissue and the nearest vessel after perturbation: $d_{max,p}^{(i)} = \max_{\mathbf{x}\in t_i}\{d_p(\mathbf{x})\}$
- Average increment of tissue-vessel distance after perturbation: $\langle \Delta d^{(i)} \rangle = \frac{\int_{t_i} \mathrm{d}\mathbf{x} \left[ d_p(\mathbf{x}) - d(\mathbf{x}) \right]}{\int_{t_i} \mathrm{d}\mathbf{x}}$
- Increase of maximum tissue-vessel distance: $\Delta d_{max}^{(i)} = d_{max,p}^{(i)} - d_{max}^{(i)}$

### Node features

The node connected components contained one or more skeleton voxels and were stored as unordered set of skeleton voxel coordinates:

$$N_i = \left\{\mathbf{x}_1^{(i)}, \mathbf{x}_2^{(i)}, \ldots \mathbf{x}_{n_i}^{(i)}\right\} \tag{9}$$

- Branch to the nearest node: number of vessel segments in the shortest path from node $i$ to its nearest node in 3D space
- Maximum, median, and minimum branch angles between link tangent vectors: $\phi_{t,max}$, $\phi_{t,med}$, $\phi_{t,min}$ were the largest, median and smallest angle (in degree) between the tangent vectors of the vessel segments (link) endpoints that connected to node $N_i$
- Maximum, median, and minimum branch angles between link end-to-end vectors: $\phi_{e,max}$, $\phi_{e,med}$, $\phi_{e,min}$ were the largest, median and smallest angle (in degree) between end-to-end vectors of the vessel segments (link) that connected to node $N_i$
- $\left| \hat{n}_{t12} \cdot \mathbf{v}_{t3} \right|$: The tangent vectors of the two connected endpoints were used to define the normal unit vector $\hat{n} = \frac{\mathbf{v}_{t1} \times \mathbf{v}_{t2}}{\| \mathbf{v}_{t1} \times \mathbf{v}_{t2} \|_2}$. The absolute value of the inner product between the normal unit vector $\hat{n}$ and the third tangent vector $\mathbf{v}_{t3}$ quantified the how close the connected vessel branches were on the same plane.

### 240-cube features

Vessel segments were extended objects that might be partially present inside the 240-cube. For a 240-cube with $n_E$ vessel segments passing by:

Please cite this article in press as: Ji et al., Brain microvasculature has a common topology with local differences in geometry that match metabolic load, Neuron (2021), https://doi.org/10.1016/j.neuron.2021.02.006



- Vessel length density: $\rho_l = \frac{1}{V_c}\sum_i^{n_E} l_i f_i$, where $f_i$ was the fraction of vessel skeleton voxels inside the bounding box of the 240-cube and $V_c$ was the volume of the 240-cube ($V_c = 240^3\ \mu m^3$)
- Capillary length density: $\rho_{lc} = \frac{1}{V_c}\sum_i^{n_E} l_i f_i Q_i$
- Similarly, the vessel (capillary) surface area density and volume density could be defined
- $\overline{d}$: Average distance transform value over the extravascular space in the cube.
- $\overline{d_{max}}$: average value of the DT local maxima inside the cube. Local extrema of $d(\mathbf{x})$ were found by a 50 $\mu m$ width moving maximum filter.

## Local vascular network anisotropy

The end-to-end vectors of the vessel segments inside the 240-cubes were used to quantify the network anisotropy. The end-to-end vector represents the net orientation of the vessel segment, as it equals the integral of the vessel tangent vector along the segment. The volume of a 240-cube is about an order of magnitude larger than the iter-vessel distance, while relatively small compare to the brain structures.

For vessel segment $i$, the volume-weighted orientation vector was $V_i\mathbf{v}_e^{(i)}$. As the order of two segment endpoints were assigned randomly, $-V_i\mathbf{v}_e^{(i)}$ was also the volume-weighted orientation vector of segment $i$. To remove the randomness in endpoint assignment, the volume-weighted orientation matrix of the $N$ vessels was a 2N-by-3 matrix with each column sum to 0:

$$M = \begin{bmatrix} \\ \mathrm{V}_1\left(\mathbf{v}_e{}^{(1)}\right)^T \\ \cdots \\ \mathrm{V}_\mathrm{N}\left(\mathbf{v}_e{}^{(N)}\right)^T \\ -\mathrm{V}_1\left(\mathbf{v}_e{}^{(1)}\right)^T \\ \cdots \\ -\mathrm{V}_\mathrm{N}\left(\mathbf{v}_e{}^{(N)}\right)^T \\ \end{bmatrix} \tag{10}$$

The 3-by-3 correlation matrix $C$ was computed as $M^TM/(2N-1)$, from which the three eigenvalue $\lambda_1$, $\lambda_2$ and $\lambda_3$ were obtained. The preferred orientation of the local vascular network was given by the eigenvector corresponded to the largest eigenvalue, while fractional anisotropy (FA) was used to quantify the absolute anisotropy level of the network:

$$\mathrm{FA} = \sqrt{\frac{1}{2}}\frac{\sqrt{(\lambda_1-\lambda_2)^2+(\lambda_2-\lambda_3)^2+(\lambda_3-\lambda_1)^2}}{\sqrt{\lambda_1^2+\lambda_2^2+\lambda_3^3}} \tag{11}$$

For isotropic network, as $N\to\infty$, $\lambda_1=\lambda_2=\lambda_3=1/3$, and therefore FA = 0, while if all the vessel segments were along one direction, FA = 1. For finite $N$, the statistical significance of network anisotropy was quantified by Monte Carlo sampling. The same volume-weights were assigned to $N$ unit orientation vectors randomly sampled from the surface of a unit sphere to compute FA. The sampling was repeated for 10000 times, and the resulting null hypothesis distribution was used to compute the z-score $\mathrm{FA_z}$ and p value $\mathrm{FA_p}$ of the local vascular network. For visualizing p value in log scale, $FA_p < 10^{-4}$ was set to be $5\times10^{-5}$.

## Regional bond percolation transition

For each brain region in each hemisphere, a vessel graph was reconstructed and reduced to an undirected graph. A fraction of edges in the graph were randomly removed according to a removal fraction $p$, and the fraction of nodes in the largest graph connected component $s(p)$ was computed. The process was repeated for 500 times for each removal fraction and each region. The percolation transition threshold was computed as the value of removal fraction $p$ that maximize $|ds/dp|$.

## Geometric scaling relations

Suppose vascular network is a cubic lattice with segment length $l$ that fills a chuck of tissue of length $L$, the volume of the tissue is $L^3$, the total length of the vessels is $L_{tot} = 3L^3/l^2$, and the vessel length density $\rho_L$ is therefore $3/l^2$. The average distance between any point in the space to the nearest edge could be calculated as:

$$\overline{d} = \frac{\int_0^{l/2}dx\int_0^{l/2-x}dy\int_0^{l/2-x}dz\sqrt{y^2+z^2}}{\int_0^{l/2}dx\int_0^{l/2-x}dy\int_0^{l/2-x}dz} = \frac{\sqrt{2}+\sinh^{-1}(1)}{8}l, \tag{12}$$

and therefore

$$\overline{d} = \frac{\sqrt{3}\left(\sqrt{2}+\sinh^{-1}(1)\right)}{8}\rho_L^{-1/2} = 0.497\rho_L^{-1/2} \tag{13}$$

Please cite this article in press as: Ji et al., Brain microvasculature has a common topology with local differences in geometry that match metabolic load, Neuron (2021), https://doi.org/10.1016/j.neuron.2021.02.006





The distance between tissue and its nearest vessel is maximized at the center of each cube, and therefore the DT maximum is $d_{max} = \sqrt{2}l/2$, and its relation with vessel length density is:

$$d_{max} = \sqrt{\frac{3}{2}}\rho_L^{-1/2} = 1.225\rho_L^{-1/2} \tag{14}$$

Though derived for cubic lattice, we expected the scaling relation $d_{max} \propto \rho_L^{-1/2}$ to hold for any regular space-filling networks, while the slope $n$ depends on specific network geometry, indicating how well a network can reduce the maximum distance between tissue and vessels, given the same length density. Moreover, if we consider vessels of finite radius $r_0$, then as $d_{max}$ is the distance between tissue and the vessel wall, we have:

$$d_{max} = n\rho_L^{-1/2} - r_0 \tag{15}$$

For regular degree-3 lattices, the slopes for the scaling relations are numerically computed from their three-dimensional reconstruction. For all these regular lattices, $d_{max} = \overline{d_{max}}$ in the main text. Equation 15 is Equation 1 in the main text and is used for the fitting in Figure 6F.

### Diffusive substrate transport and consumption

Consider steady state metabolic substrate exchange between vessel and tissue through diffusion. By assuming constant substrate concentration on vessel wall, tissue metabolism rate $k$, and diffusion coefficient $D$, the concentration difference between the tissue and vessel wall $\Delta c(\mathbf{r})$ in the tissue at $\mathbf{r} = (x, y, z)$ can be described by the Poisson equation:

$$\begin{cases} \nabla^2(\Delta c(\mathbf{r})) = \dfrac{k}{D}, & \mathbf{r} \in \Omega_{tissue} \\ \Delta c(\mathbf{r}) = 0, & \mathbf{r} \in \partial\Omega_{vessel} \end{cases} \tag{16}$$

Concentration depends on metabolism rate, vessel geometry, and diffusion rate. However, Equation 16 is linear, with a constant inhomogeneous term and a constant Dirichlet boundary condition. Therefore, we can solve the following equation for the "normalized concentration difference" $u(\mathbf{r})$:

$$\begin{cases} \nabla^2 u(\mathbf{r}) = 1, & \mathbf{r} \in \Omega_{tissue} \\ u(\mathbf{r}) = 0, & \mathbf{r} \in \partial\Omega_{vessel} \end{cases} \tag{17}$$

and obtain $\Delta c(\mathbf{r})$ by a linear transformation:

$$\Delta c(\mathbf{r}) = \frac{k}{D} u(\mathbf{r}) \tag{18}$$

In other words, under our assumption, the effects of network geometry on tissue substrate concentration can be separated from properties specific to the substrates ($k$, $D$ and $c_0$).

We numerically solved Equation 17 using iterative multi-scale finite difference method. The numerical solutions were obtained for the reconstructed vessel mask at different resolutions. Solutions from lower resolution were interpolated to initialize the solution at higher resolutions. The final resolution of 2 $\mu m$ was a compromise between relevant scale of capillaries, target precision and the computation resource. At each resolution, iteration was terminated when the maximum relative update was less than $1\times 10^{-6}$ or the maximum iteration number (20000) was reached. At 2 $\mu m$ voxel resolution, the solution near vessel wall was not accurate, but our analysis focused on the local concentration minimum. For a typical tissue volume, $u(\mathbf{r})$ calculated from 1 $\mu m$ and 2 $\mu m$ resolution only differed by less than 3% for tissues more than 20 $\mu m$ away from the vessel wall. The maximum iteration number was set such that the characteristic diffusion distance is about an order of magnitude longer than the typical inter-capillary distance. The brain was divided into cubes of length 816 $\mu m$ and each cube had 160 $\mu m$ overlap with its 6-neighbors. Adiabatic boundary condition was applied on the system boundary, and the overlapping volume (80 $\mu m$ on each side) was necessary for eliminating the boundary effect. The solutions in these 816$\mu m$-cubes were divided backed into 240-cubes for the following analysis.

We assumed the tissue metabolism rate $k$ to be the same within each 240-cube, as 240 $\mu m$ is smaller than the scale of typical anatomical regions that could be resolved by metabolic measurements in the brain. We used a 50 $\mu m$ square moving window to search for local normalized concentration minima $u_{min} = \Delta c_{min} D/k$ at $\mathbf{r}_{u_{min}}$ in each 240-cube. Note that under this assumption, the locations of $u(\mathbf{r})$ local minima are exactly the same as $\Delta c(\mathbf{r})$'s (i.e., $\mathbf{r}_{u_{min}} = \mathbf{r}_{c_{min}}$). The distance transform was used to compute the distance between each local concentration minima and its nearest vessel wall $d_{c_{min}} = d(\mathbf{r}_{u_{min}})$. For each 240-cube, we compute the average of local concentration minimum value $\overline{u_{min}}$ and the average distance between local concentration minima and their nearest vessel wall $\overline{d_{c_{min}}}$.

A critical observation is that, under our assumptions, $u(\mathbf{r})$ tends to be minimized at the places that $d(\mathbf{r})$ is maximized. Note that though this is intuitively true for some simple system geometries, in general it is not the case. A simple counterexample is:

$$\begin{cases} \dfrac{d^2c(r)}{dr^2}+\dfrac{1}{r}\dfrac{dc(r)}{dr}=k, \quad r\in[R_1,R_2], \\ c(R_1)=c(R_2)=c_0, \end{cases} \tag{19}$$

whose concentration is minimized at

$$r_c=\sqrt{\frac{R_1^2-R_2^2}{2\log(R_1/R_2)}} \tag{20}$$

but the shortest distance to either cylinder is maximized at $(R_1+R_2)/2$. However, with the solutions of both $d(\mathbf{r})$ and $u(\mathbf{r})$ in 91751 240-cubes across 3 brains, we found $\overline{d_{c_{min}}}=1.001\overline{d_{max}}$ (Equation 2 in the main text) with $R^2=0.88$ (Figure 7C). The dependence of this approximation on the window size used for searching the local extrema was further analyzed and shown in Figure S5.

We then looked for an analytical formula to approximately relate $\overline{u_{min}}$ with $\overline{d_{max}}$. First, notice that generally $u(\mathbf{r})$ deceases as $d(\mathbf{r})$ increases (Figure 7B), but the spread of the joint distribution indicates the complexity of the numerical solution due to the vascular network geometry. Second, at local concentration minima, the concentration gradient vanishes ($\nabla u(\mathbf{r}_{u_{min}})=0$), and so does the diffusion flux. Therefore, we looked for a formula that (a) describes substrate diffusion from vessels wall, (b) has concentration minimized at $\overline{d_{c_{min}}}$, and (c) has a maximum tissue-vessel concentration difference $\overline{u_{min}}$.

The Krogh model (Krogh, 1919) is a special case of Equation 16, where one infinitely long cylindric vessel of radius $r_0$ presents in the tissue, and the concentration reaches a minimum level $c_{min}$ at tissue $d_{c_{min}}$ away from the vessel wall:

$$\begin{cases} \dfrac{1}{r}\dfrac{d}{dr}\left(r\dfrac{dc}{dr}\right)=\dfrac{k}{D}, \quad r\in(r_0,r_{max}) \\ c(r_0)=c_0, \\ \dfrac{dc}{dr}|_{r=r_{max}}=0, \end{cases} \tag{21}$$

where $r_{max}=d_{c_{min}}+r_0$. The solution gives the maximum substrate concentration difference between tissue and vessel as:

$$\Delta c(r_{max})=\frac{k}{D}\left[-\frac{r_{max}^2}{2}\log\left(\frac{r_{max}}{r_0}\right)+\frac{r_{max}^2-r_0^2}{4}\right]=\frac{k}{D}u(r_{max}). \tag{22}$$

Note that Equation 22 takes the same form as Equation 18 and terms inside the squared bracket $u(r_{max})$ completely depend on the vessel geometry. The Krogh model was derived for vessels in the mussel, where capillaries are aligned along one direction with relatively uniform spacing. Brain capillary network is far less regular, and our numerical solution suggested that $u(\overline{d_{max}}+r_0)$ calculated from Equation 22 is about 100% higher than $\overline{u_{min}}$. Nonetheless, Equation 22 provides a simple relation between concentration difference and vessel geometries for substrates transported through diffusion. To reconcile the quantitative difference, we used Equation 22 as a "functional form" to fit $\overline{u_{min}}$ with respect to $\overline{d_{max}}$ using linear regression, and denote the slope as $\lambda$:

$$\overline{u_{min}}=-\frac{\lambda}{2}\left[r_{max}^2\left(\log\left(\frac{r_{max}}{r_0}\right)-\frac{1}{2}\right)+\frac{r_0^2}{2}\right], \tag{23}$$

where $r_{max}=\overline{d_{max}}+r_0$. This is the equation used for fitting $\lambda$ in Figure 7D. For 91751 240-cubes across 3 brains, the fitting yielded $\lambda=0.5185$ with $R^2=0.897$. Note that Equation 23 relates normalized concentration difference to vascular network geometrical parameters, and is independent of substrate properties and metabolism rate. The accuracy of the fitting suggests that the functional form of the Krogh model capture most of the dependence of $\overline{u_{min}}$ on $\overline{d_{max}}$, while $\lambda$ captures the shared structural properties of the vascular network across the brain. The Krogh model describes diffusion from a single vessel segment, while $\lambda$ is a structural parameter that relates the single vessel solution to the vascular network solution (*only for the local extrema*).

We applied Equation 23 for oxygen transportation in the brain under homeostasis. Using Equation 18, the oxygen consumption rate $k_{O_2}$ can be expressed as:

$$k_{O_2}=\frac{2\alpha_{O_2}D_{O_2}}{\lambda\left[r_{max}^2\left(\log\left(\frac{r_{max}}{r_0}\right)-\frac{1}{2}\right)+\frac{r_0^2}{2}\right]}\Delta pO_2, \tag{24}$$

where oxygen concentration has been converted to partial pressure through oxygen solubility $\alpha_{O_2}$, and $\Delta pO_2$ is the oxygen partial pressure difference between vessel wall and tissue oxygen partial pressure minimum.

Furthermore, using the scaling relation between $d_{max}$ and vessel length density Equation 15, and the oxygen-glucose index $\kappa=k_{O_2}/k_{glu}$, we obtained a relation between vessel length density and glucose metabolism rate:

$$k_{glu} = \frac{4\alpha_{O_2} D_{O_2}}{\kappa\lambda} \frac{\rho_L}{n^2\left[\log(n^2) - 1 - \log\left(r_0^2\rho_L\right)\right] - r_0^2\rho_L} \Delta pO_2$$
$$\approx \frac{4\alpha_{O_2} D_{O_2}}{\kappa\lambda} \frac{\rho_L}{n^2\left[\log(n^2) - 1 - \log\left(r_0^2\rho_L\right)\right]} \Delta pO_2, \quad (25)$$

where we took the limit of $\rho_L r_0^2 \ll 1$ in the last step. Note that in the denominator the logarithmic term in $\rho_L$ grows slowly, and therefore, regional glucose metabolism rate $k_{glu}$ is approximately linear in vessel length density $\rho_L$ if $\Delta pO_2$ is held a constant. This is the Equation 3 visualized in Figures 7E and 7F.

## Reported statistics

- Figure 1J: For each 240-cube, we compute the fraction of the included vessel segments with at least one unconnected endpoint. This fraction is computed for the internal 3 × 3 × 3 240-cubes in a 1072-cube, and the "included" vessel segments has at least one centerline voxel inside the 240-cube. Figure 1J shows the cumulative probability density function of this fraction for all the 240-cubes inside three brains separately.
- Figures 3C–3E: For each 240-cube, we compute the probability density functions of the features. For a given feature, the PDFs of 105,252 240-cubes in 3 brains are merged directly to compute the boxplots. Each whisker shows the distribution of probability density for the feature within the range specified by the binning edges. The maximum whisker length is computed as $1.5\times(q_3 - q_1)$ by default, where $q_1$ and $q_3$ are the 25th and 75th percentiles, respectively. Outliers are not shown.
- Figure 3F: For each brain, the probability density function of the vessel segment radius is computed and plotted as solid dots. These probability density functions are computed with the same bins of radius, and therefore are used to directly compute the average probability density and the standard deviation, for each radius bin, as shown in the purple solid curve and the shadow patch.
- Figure 3G: For each brain, the probability density function of the capillary branch order is computed with the same bins. The plotted solid curves and the shadow patch show the mean and standard deviation of the probability density functions over 3 brains.
- Figure 3H: For each structure in each hemisphere, 500 percolation simulations are computed to obtain the average percolation transition curve. Each curve in Figure 3H is the averaged curve over 6 hemispheres. For display clarity, standard error is not shown.
- Figure 4D: For each 240-cube, we quantify network anisotropy for vessel segments of radius between 0 and $r\mu m$, where $r$ takes the values on the x axis. For each radius upper limit, data from brains are merged to generate the boxplots.
- Figure 4F: For each structure in each hemisphere, we compute the average anisotropy and median p value for all the 240-cubes inside the structure for each range of vessel segment radius. The upper panel shows the average and standard error of average anisotropy over 4 hemispheres. The lower panel shows the median and 25-75 percentiles interval of the p values across 4 hemispheres.
- Figure 4G: For each structure in each hemisphere, we compute the average projection of the principal orientation unit vector of the capillary network to the normal direction of the cortical surface across all the included 240-cube and the median of the p value. The upper panel shows the average and standard error of the average projection across 4 hemispheres. The lower panel shows the median and 25-75 percentiles interval of the p value across 4 hemispheres. The normal direction to the cortical surface is computed according to the gradient of the distance transform with respect to the brain surface.
- Figure 5B: For each structure in each hemisphere, we compute the probability density function of the capillary length density for all the 240-cubes inside the structure. Each curve and the shadow area show the mean and standard deviation over 6 hemispheres. Same method for Figures 6B and 6D.
- Figure 5C: We use the distance transform with respect to the brain surface to bin the vessel centerline at different cortical depth, and compute the capillary length density within each bin. Each curve and the shadow area show the mean and standard deviation over 6 hemispheres.
- Figure 5D: For each structure in each hemisphere, we compute the probability density function of the capillary segment length inside the structure. Each curve and the shadow area show the mean and standard deviation over 6 hemispheres. Same method for Figures 6H and 6I.
- Figure 5E: The lengths of all the vessel segments in each brain are used to compute the probability density function. The average and standard deviation of the resulting density functions are shown as solid line and shadow area, respectively.
- Figures 6C, 6E, 7C, and 7D: two-dimensional joint histogram for features in 91,751 240-cubes from 3 brains, where capillaries account for more than 50% of the vascular volume inside the cube.
- Figure 7E: For each regions in each brain, the length densities in the 240-cubes in both hemispheres are combined to compute the median and 25-75 percentiles.
- Figure 7F: For each regions, the length densities in the 240-cubes in all 3 brains are combined to compute the median and 25-75 percentiles for the rodent data points.